NAVAL POSTGRADUATE SCHOOL

MONTEREY, CALIFORNIA

THESIS

OPTIMIZATION OF ADAPTIVE DIRECT SIGNAL SUPPRESSION FOR SINGLE-CHANNEL PASSIVE RADAR SENSING

by

Athanasios Lamprou

December 2023

Thesis Advisor:	Sean T. Peters
Co-Advisor:	Christopher G. Smithtro

Approved for public release. Distribution is unlimited.

THIS PAGE INTENTIONALLY LEFT BLANK

REPORT DOCUMENTATION PAGE	*Form Approved OMB No. 0704-0188*

1. AGENCY USE ONLY ***(Leave blank)***	**2. REPORT DATE** December 2023	**3. REPORT TYPE AND DATES COVERED** Master's thesis

4. TITLE AND SUBTITLE OPTIMIZATION OF ADAPTIVE DIRECT SIGNAL SUPPRESSION FOR SINGLE-CHANNEL PASSIVE RADAR SENSING	**5. FUNDING NUMBERS**
6. AUTHOR(S) Athanasios Lamprou	
7. PERFORMING ORGANIZATION NAME(S) AND ADDRESS(ES) Naval Postgraduate School Monterey, CA 93943-5000	**8. PERFORMING ORGANIZATION REPORT NUMBER**
9. SPONSORING / MONITORING AGENCY NAME(S) AND ADDRESS(ES) N/A	**10. SPONSORING / MONITORING AGENCY REPORT NUMBER**

11. SUPPLEMENTARY NOTES The views expressed in this thesis are those of the author and do not reflect the official policy or position of the Department of Defense or the U.S. Government.

12a. DISTRIBUTION / AVAILABILITY STATEMENT Approved for public release. Distribution is unlimited.	**12b. DISTRIBUTION CODE** A

13. ABSTRACT (maximum 200 words)

This thesis optimizes a previously developed direct signal suppression (DSS) algorithm for single-channel passive radar that uses radio-astronomical sources (e.g., the sun and Jupiter's radio emissions) as ambient noises, as we first noted at the IGARSS 2023 IEEE Symposium. Such passive radars can be used in extreme environments such as polar regions to measure ice sheet thickness and space-based experiments as a low-resource solution. To optimize the DSS algorithm, we estimate the direct signal and perform Wiener deconvolution, focusing on echo peak power (α) and delay time (τ) in the impulse response function construction. Although only a minor increase in signal-to-noise ratio (SNR) was achieved compared to the previous approach, the results highlight the significant losses in SNR if the estimation of the phase (τ) is not accurate. On the other hand, the amplitude of the impulse response has a negligible impact on SNR compared to the correct phase estimation. The latter part of this thesis focuses on the Total Electron Content (TEC) of Earth's ionosphere over Greenland and explores its variations across different timescales, including daily, yearly, and solar cycles. Based on these calculations, the phase difference and the time delay generated due to the TEC are presented. Significantly, the study evaluates the potential impact of inadequately accounting for TEC on the SNR of a space-based single-channel passive radar orbiting in a Low Earth Orbit (LEO) above Greenland.

14. SUBJECT TERMS space-based passive radar, adaptive signal processing, single channel direct signal suppression, optimization of SNR	**15. NUMBER OF PAGES** 89
	16. PRICE CODE

17. SECURITY CLASSIFICATION OF REPORT Unclassified	**18. SECURITY CLASSIFICATION OF THIS PAGE** Unclassified	**19. SECURITY CLASSIFICATION OF ABSTRACT** Unclassified	**20. LIMITATION OF ABSTRACT** UU

NSN 7540-01-280-5500

Standard Form 298 (Rev. 2-89)
Prescribed by ANSI Std. 239-18

THIS PAGE INTENTIONALLY LEFT BLANK

OPTIMIZATION OF ADAPTIVE DIRECT SIGNAL SUPPRESSION FOR SINGLE-CHANNEL PASSIVE RADAR SENSING

Athanasios Lamprou
Lieutenant, Hellenic Navy
BS, Hellenic Naval Academy, 2010
MS, National Technical University of Athens, 2017

Submitted in partial fulfillment of the
requirements for the degrees of

MASTER OF SCIENCE IN APPLIED PHYSICS

and

MASTER OF SCIENCE IN SPACE SYSTEMS OPERATIONS

from the

NAVAL POSTGRADUATE SCHOOL
December 2023

Approved by: Sean T. Peters
Advisor

Christopher G. Smithtro
Co-Advisor

Frank A. Narducci
Chair, Department of Physics

James H. Newman
Chair, Space Systems Academic Group

THIS PAGE INTENTIONALLY LEFT BLANK

ABSTRACT

This thesis optimizes a previously developed direct signal suppression (DSS) algorithm for single-channel passive radar that uses radio-astronomical sources (e.g., the sun and Jupiter's radio emissions) as ambient noises, as we first noted at the IGARSS 2023 IEEE Symposium. Such passive radars can be used in extreme environments such as polar regions to measure ice sheet thickness and space-based experiments as a low-resource solution. To optimize the DSS algorithm, we estimate the direct signal and perform Wiener deconvolution, focusing on echo peak power (α) and delay time (τ) in the impulse response function construction. Although only a minor increase in signal-to-noise ratio (SNR) was achieved compared to the previous approach, the results highlight the significant losses in SNR if the estimation of the phase (τ) is not accurate. On the other hand, the amplitude of the impulse response has a negligible impact on SNR compared to the correct phase estimation. The latter part of this thesis focuses on the Total Electron Content (TEC) of Earth's ionosphere over Greenland and explores its variations across different timescales, including daily, yearly, and solar cycles. Based on these calculations, the phase difference and the time delay generated due to the TEC are presented. Significantly, the study evaluates the potential impact of inadequately accounting for TEC on the SNR of a space-based single-channel passive radar orbiting in a Low Earth Orbit (LEO) above Greenland.

THIS PAGE INTENTIONALLY LEFT BLANK

TABLE OF CONTENTS

LIST OF FIGURES

LIST OF TABLES

THIS PAGE INTENTIONALLY LEFT BLANK

LIST OF ACRONYMS AND ABBREVIATIONS

CPI	Coherent Processing Interval
DAB	Digital Audio Broadcasting
dB	Decibel
DPI	Direct Path Interference
DSI	Direct Signal Interference
DSS	Direct Signal Suppression
DVB-T	Terrestrial Digital Television
FY	Fiscal Year
GNSS	Global Navigation Satellite System
GPS	Global Positioning System
IEEE	Institute of Electrical and Electronics Engineers
IGARSS	International Geoscience and Remote Sensing Symposium
IRI	International Reference Ionosphere
JUNO	Jupiter’s Near polar Orbiter
LPD	Low Probability of Detection
LPI	Low Probability of Intercept
LTI	Linear Time-Invariant
LWA	Long Wavelength Array
RADAR	RAdio Detection And Ranging
RAM	Radar Absorbing Material
RCS	Radar Cross Section

REASON	Radar for Europa Assessment and Sounding: Ocean to Near-surface
RF	Radio Frequency
RIME	Radar for Icy Moon Exploration
SAR	Synthetic Aperture Radar
SNR	Signal-to-Noise Ratio
STEC	Slant Total Electron Content
TDOA	Time Difference Of Arrival
TEC	Total Electron Content
UTC	Universal Coordinated Time
VTEC	Vertical Total Electron Content
WGN	White Gaussian Noise

ACKNOWLEDGMENTS

First of all, I would like to express my appreciation to my thesis advisor, Dr. Sean Peters, and my co-advisor, Dr. Christopher Smithtro, for the valuable guidance and assistance they provided to me throughout my work. Also, their leading figures motivated me to reach new heights in my research and academic pursuits. I am truly grateful for their mentorship and encouragement throughout this journey.

Furthermore, I would like to express my gratitude to the Hellenic Navy for granting me the opportunity to pursue my dual master's degree in the U.S. I am also thankful to Naval Postgraduate School for its hospitality, the exceptional level of education that it provides, and the remarkable professionalism that characterizes both faculty and staff.

To my beloved parents and sister, thanks for all the love that you surround me with all these years and the concrete foundations you have provided me for every achievement in my life.

Last but certainly not least, I express my deepest gratitude to my beloved wife Eleni and our precious twins Dimitra and George, for their love, encouragement, support, and patience throughout these years. Words fail to capture the depth of my appreciation. I love you so much! Thank you!

THIS PAGE INTENTIONALLY LEFT BLANK

I. INTRODUCTION

A. ACTIVE VERSUS PASSIVE RADAR

Radars (RAdio Detection and Ranging) stand as one of the most remarkable technological achievements of the 20th century. Even though the first applications of radar systems were in the military sector, having their roots in World War II, many other applications took place throughout the years, making radars a valuable tool in various fields, from aviation and meteorology to medicine and maritime navigation. Radars utilize radio waves to detect, locate, and track objects in the vast expanses of the atmosphere and beyond. In its more simplistic version, traditional radar, also known as active radar, transmits an electromagnetic pulse in the air and receives a reflection of the pulse from the target of interest. The time between sending and receiving the signal is then translated into the distance or range of the target. In a slightly more sophisticated version, radars can provide valuable information such as the direction, speed, and altitude of the target. Active radars are essential in modern militaries, providing critical surveillance, defense, targeting, and strategic decision-making capabilities. Applications such as surveillance and detection, air defense, targeting, fire control, navigation, and space situational awareness make radars a crucial tool in all modern war-fighting domains. Although traditional radars were the first to be introduced, many other variations have been invented over the ages, including the passive radar.

Passive radars encompass remote sensing technologies capable of detecting, monitoring, and tracking targets of interest without transmitting any electromagnetic pulse, instead depending on ambient radio emissions from radio frequency sources, either anthropogenic or natural, in the surrounding environment [1], [2]. There are many ways that passive radars can be beneficial to the military. Advantages of passive over active radars, such as stealth and covert operations, reduced vulnerability, and low probability of intercept (LPI) are only a couple of those. Modern battlefields, in all war-fighting domains, comprise congested electromagnetic radiation environments. Taking this into account and given the fact that the electromagnetic spectrum is finite, passive radars are systems that the U.S. Navy and the other U.S. branches can benefit from. It is important to note that although the most widely used term is “passive radar,” passive covert radar, or PCR, and passive coherent location, or PCL, are also encountered, especially by users in the military sector [1].

Figure 1 provides an example of a space-based passive radar that uses the emissions of the Sun or Jupiter as an ambient noise source and receives the electromagnetic signal reflected from the target of interest, represented by the red dashed line. The black dashed line from the Sun towards the satellite represents the direct path signal captured by the reference component of the radar, while the rest of the black lines represent potential noise in the environment.

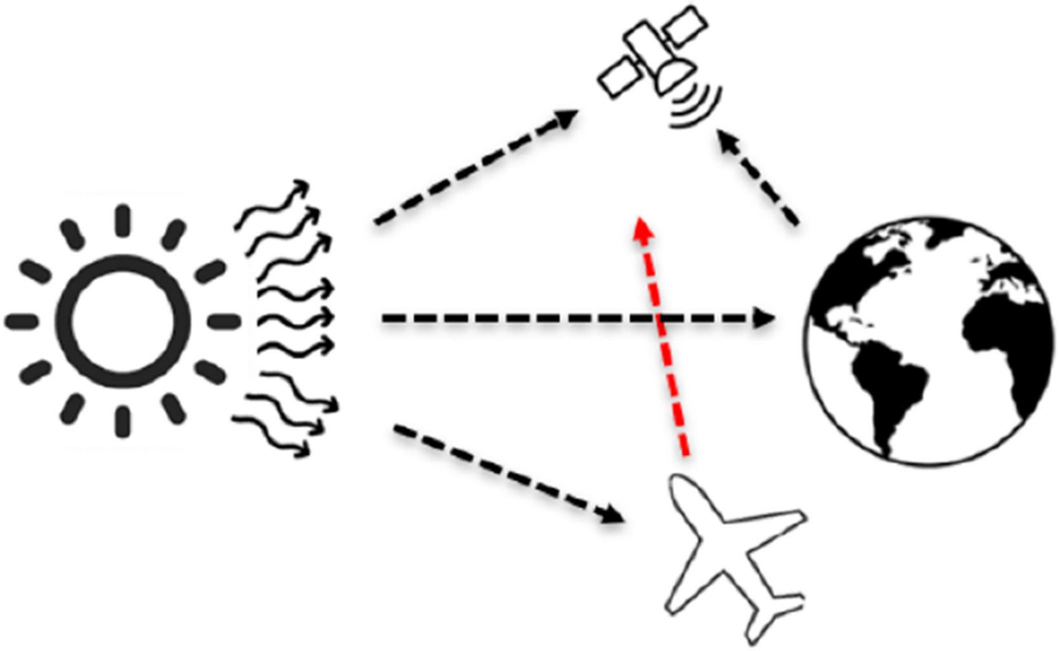

Natural ambient radio waves are received directly from an illumination source (i.e., the Sun), from undesired reflections on the surface of random objects (i.e., Earth’s surface) and reflections from an object of interest (i.e., air target).

Figure 1. Example of Space-Based Passive Radar. Source: [2].

B. ADVANTAGES OF PASSIVE RADARS

Several advantages of passive radars over their counterpart, active radar, make their use appealing in modern applications. Of course, active radars are also superior to passive radars in other applications. Therefore, from one perspective, a combined use of them can provide the optimum result. A brief list of the advantages of passive radars is shown:

- Reduction in complexity because the radar consists of fewer parts than a conventional radar, as one of the more complex components, the transmitter, is not needed.
- Overall reduction of the procurement, operation, and maintenance costs, as fewer parts are needed.
- Less energy is needed to operate, as the radar does not transmit, which often is the most power consuming aspect of a radar.
- Covert operation, also known as Low Probability of Detection (LPD).
- Operation in spectrum congestion: As the electromagnetic spectrum becomes more crowded, passive radars do not use separate parts of the electromagnetic spectrum but only existing signals of opportunity.
- Vulnerability reduction: As they do not transmit signals, they are less vulnerable to electronic attack measures (EA) or electronic countermeasures (ECM). Jamming must be distributed across various directions and in a broad part of the spectrum, which will reduce their overall effectiveness.
- Unlike active radars, which require a license to transmit at a given frequency, passive radar does not require a license since nothing is transmitted.
- In many cases, passive radars can be more effective in the detection of stealthy targets, as they can have bistatic and multistatic configurations, where multiple receivers are used to detect the same target from different angles, allowing for accurate target localization and tracking, even for targets with a low RCS (Radar Cross Section) that might not return a strong radar reflection.

C. APPLICATIONS OF PASSIVE RADARS

Applications of passive radars can be found in the military and the commercial world. However, this area is still evolving with new applications. A few modern applications of passive radars include:

- Air traffic control and surveillance [3]
- Maritime detection and surveillance [4]
- Passive Synthetic Aperture Radars (SAR) [5]
- Space debris detection and tracking [6], [7]
- Indoor surveillance systems [1]
- Ocean Scatterometry Using GNSS (Global Navigation Satellite System) Signals [1]
- Terrestrial Bistatic Weather Radar [1]
- Planetary Radar Remote Sensing [1], [2], [8], [9]. An overview of one of the research projects done in this field is presented in Figure 2, where a space-based passive radar orbits a planet, potentially a moon of Jupiter, and receives the direct path signal, a radio burst from the interaction of Jupiter with Io, and at the same time receives the echoes of this signal after being reflected by the planet. After comparing the two signals, the radar can distinguish the reflected from the direct emissions using autocorrelation methods and then provide useful measurements about the planet's surface.

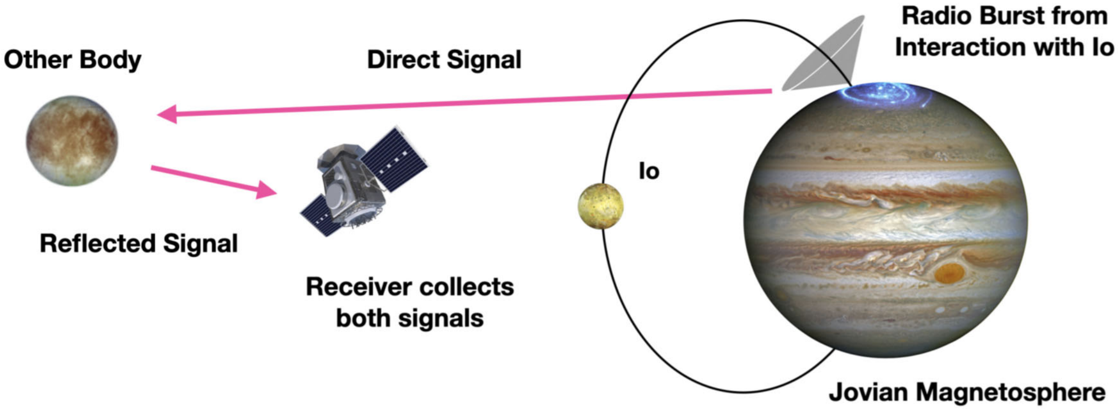

A space-based passive radar uses radio bursts from interaction with Io as ambient noise and receives the direct and reflected signal. By autocorrelation techniques, the radar eliminates the direct emissions and can then provide measurement of the surface of the planet.

Figure 2. Example of Passive Radar Sounding Using Jovian Radio Bursts. Source: [10].

Although there are many examples of passive radars in use, a significant number of applications still need development. Furthermore, it is essential to note that passive radars are complementary to equivalent active radars in many applications.

D. MOTIVATION

Passive radars offer unique advantages that complement the Navy's radar capabilities and operational strategies. They can enhance situational awareness, increase operational effectiveness, and contribute to the success of a wide range of naval missions, which motivates future research in this field.

For this research, we are interested in developing a low-resource radar system for deployment in remote areas such as Greenland and Antarctica to measure how ice sheets change during the year and estimate their thickness, melting rates, and morphology. The motivation for using a passive radar instead of an active radar is the overall reduction in energy consumption needed to operate and the lower need for logistics to support the mission. Since there are few sources of radio emissions in the polar regions, we explored using solar emissions.

However, there are tradeoffs in using a passive radar. The low Signal-to-Noise-Ratio (SNR) is one major drawback of passive radars. Therefore, our goal was to optimize the direct path interference algorithm for two different scenarios: a stationary case and a moving platform. The desired end-state is a low-resource asset that can operate with no architecture modification and be used in future space-based and interplanetary missions.

E. THESIS ORGANIZATION

The objective of this research is (1) the optimization of a signal processing algorithm used in a single-channel passive radar to measure the thickness of ice sheets in polar regions and (2) to investigate the effects of phase errors generated from the total electron content (TEC) when the signal propagates through the ionosphere in the case of space-based assets. The structure of this thesis is comprised of five chapters in total. It starts with the current chapter, briefly introducing and motivating the research. Chapter II provides a more extended discussion of passive radar theory, different types of passive radars, and typical signal processing algorithms. Chapter III covers the first main objective of the thesis, the optimization of the direct signal suppression algorithm. It provides further background and discusses the findings. Chapter IV covers the second thesis objective, calculating the effects of TEC of ionosphere to the shift of the phase of the signal, and relate this to results from Chapter III for a space-based platform. Finally, Chapter V summarizes this research’s findings and suggests potential improvements for future work.

II. BACKGROUND

A. PASSIVE RADARS

The evolution of radar systems is remarkable, when one compares the first inventions and applications that were limited to target detection to state-of-the-art radars. Today's radars comprise sophisticated computer systems capable of detecting and imaging targets while operating in a jamming environment. Modern applications of radars expand in a wide range, from military to civilian uses and from the traditional detection of targets like ships and aircrafts to two- and three-dimensional mapping, space debris tracking, space situational awareness and collision avoidance. To succeed in those new applications, different types of traditional radar have been invented and developed, including passive radar.

The first experimental applications of passive radars date back to the 1920s in England, using the British Broadcasting Corporation (BBC) radio emissions for illumination. The first passive radar application was the German *Klein Heidelberg* radar in 1943, shown in the left panel of Figure 3. However, the applications for conventional radars expanded much faster than passive radars because, as one can easily see from the left side of Figure 3, the first passive radars were quite large in size, making them hard to handle and place on platforms other than the ground. Of course, the first applications of active radars were quite big as well, but other reasons contributed to traditional radars expanding more rapidly than passive radars. The right side of Figure 3 presents applications of modern passive radars. At the top right panel, Hensoldt's TwinVis passive radar system for air defense is shown, while the bottom right panel presents the Silentium Defense Maverick S-series air and space search passive radar.

(Left) Antenna of Klein Heidelberg. The first application of a passive radar was in the 1940s. Source: [11]. (Right) Antennas of modern passive radars. At the top right panel, Hensoldt's TwinVis passive radar system for air defense is presented, while the bottom right panel shows the Silentium Defense Maverick S-series air and space search radar.

Figure 3. Antennas of Passive Radars. Source: [12].

To understand passive radars, it is first important to familiarize oneself with the system's geometry in addition to essential parts and definitions. Figure 4 presents one simplistic version of a passive radar. In this, one can see the main components that encompass a passive radar. The depicted antennas, reference, and surveillance are the two main parts of the passive radar. Moreover, the broadcasting antenna plays the role of the non-cooperative illumination source, which transmits electromagnetic signals in all directions. The emissions from this source arrive through different paths at the surveillance antenna: directly, after being reflected onto various objects or the ground, forming the clutter, and finally, after being reflected on the target. Also, as depicted by the dashed line, the reference antenna receives direct emissions from the illumination source. After following various techniques, the radar subtracts the direct path from the signal captured from the surveillance antenna and then processes the information about the desired target [1], [2], [14].

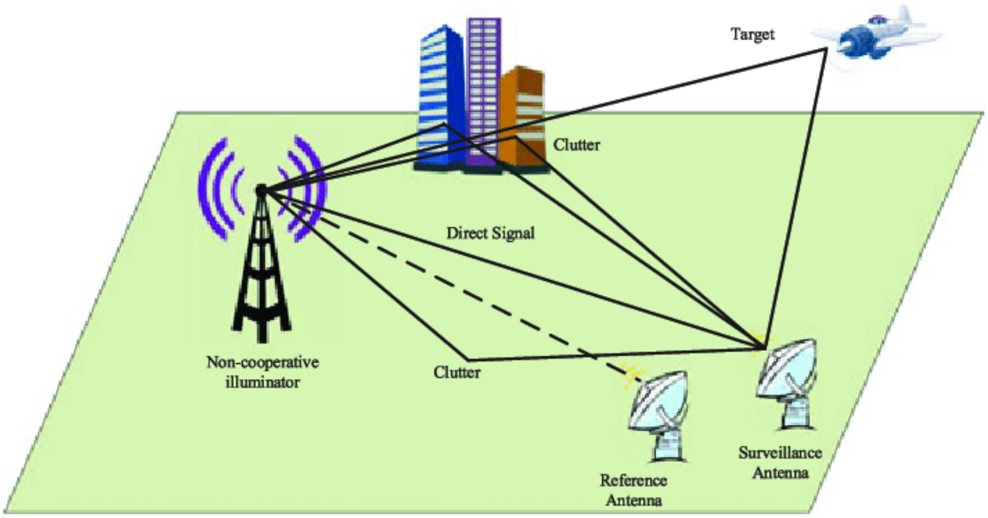

The fundamental components of passive radar include the reference and surveillance antenna. In this setup, the broadcasting antenna is a non-cooperative illumination source, emitting electromagnetic signals in all directions. These emissions travel through different paths to reach the surveillance antenna: some directly, while others are reflected off objects or the ground, creating clutter, and eventually bouncing off the target. Therefore, "the signal received by the surveillance antenna includes" [2]: (1) a time-delayed direct signal (the delay is different from the equivalent time delay in the reference channel and depends on the distance to the location of the illuminator), (2) signals that correspond to multipath propagation, (3) clutter reflections, and finally, (4) the signal that corresponds to the reflection of the target. At the same time, as depicted by the dashed line, the reference antenna detects the direct emissions from the illumination source. Employing specialized methods, the radar system deducts "the signal received directly by the surveillance antenna from the total signal." Finally, the system analyzes the remaining data to extract information about the targeted object.

Figure 4. Example of a Ground-Based Passive Radar and Its Geometry. Source: [15].

An easy way to understand passive radars is by comparing them to active radars. One significant difference between the two is regarding the transmitter. Unlike active radars, where the transmitter and the receiver are at the same location, in passive radars the transmitter is at a different location. Furthermore, it is not referred to as a transmitter but an illuminator or source of illumination since it is not controlled by the operator of the passive radar, meaning it is not cooperative.

Some passive radar systems include more than one illumination source. Since passive radars do not need a dedicated transmitter, existing sources of radio frequency (RF) signals, such as commercial broadcasts, communication signals, and emissions from celestial bodies like the Sun and Jupiter provide the source signal.

Another difference between passive and active radars is the receiver. Although both types of radars have one, passive radars usually have more than one receiver. The terms monostatic, bistatic, and multi-static are used to distinguish between passive radar systems based on the number of receivers. Single channel and multi-channel are other terms widely used to describe the same thing. Also, as shown in Figure 3, the receivers have different names because they serve different purposes. One receiver is called the reference antenna, as it estimates the direct signal and provides the reference to the other antenna, which is called the surveillance antenna, as it is used for the actual detection and monitoring of the target. The locations of the illuminating sources and receivers are called nodes.

To compute the target's position, passive radars measure the time difference between the arrival of the direct source signal and their reflections off objects or surfaces of interest for echo detection, ranging, and imaging [1]. A description of the process to compute the difference between the two signals follows. The surveillance channel receives a time-delayed signal of the transmitted signal, as depicted by the dashed line in Figure 4. Also, as shown in Figure 4, at the same time, the surveillance channel receives a signal that contains (1) a time-delayed direct signal (the delay is different from the equivalent time delay in the reference channel and depends on the distance to the location of the illuminator), (2) signals that correspond to multipath propagation, (3) clutter reflections, and finally, (4) the signal that corresponds to the reflection of the target. The range of the target corresponds to the difference between the two signals originating from the two different channels.

The signal-to-noise ratio (SNR), or the power of the received signal over the power of the noise, of a bistatic passive radar [1] is given by

$$SNR = \frac{P_T \cdot G_T}{4\pi R_T^2} \cdot \frac{G_R}{4\pi R_R^2} \cdot \frac{\sigma_b}{4\pi} \cdot \frac{\lambda^2}{kT_0BF} \tag{1}$$

where P_T is the transmit power, G_T is the gain of the transmit antenna, R_T is the range between the transmitter and the target, G_R is the receive antenna gain, R_R is the target-to-receiver range, σ_b is the target bistatic RCS, λ is the wavelength of the transmitted RF, k is Boltzmann's constant, T_0 is the noise reference temperature, 290K, B is the receiver's effective bandwidth, and F is the noise figure of the receiving system [1].

Equation (1) is important because getting the best SNR from a radar is generally the number one priority. Still, especially in this research, our primary goal is to optimize SNR with respect to some parameters and under some assumptions, as we will explore in the main body of this thesis.

One effective way to understand how equation (1) works is by providing a schematic. Figure 5 presents the Ovals of Cassini, where one can see how the time difference of arrival between the direct and the reflected signal is translated in the distance that forms the ellipses. Equation (1) calculates the SNR that corresponds to a detection of a target for a given distance. From another perspective, if one changes the variables in this equation, and for a given SNR would like to calculate the possible locations of a target, you will get the ellipses depicted in Figure 5. However, this is for the simple case of a bistatic radar. In the case of multi-static radars, this set of ellipses intervenes with another group of ellipses, due to the other transmitter/receiver pair, enabling the triangulation that provides the exact position within an area of uncertainty.

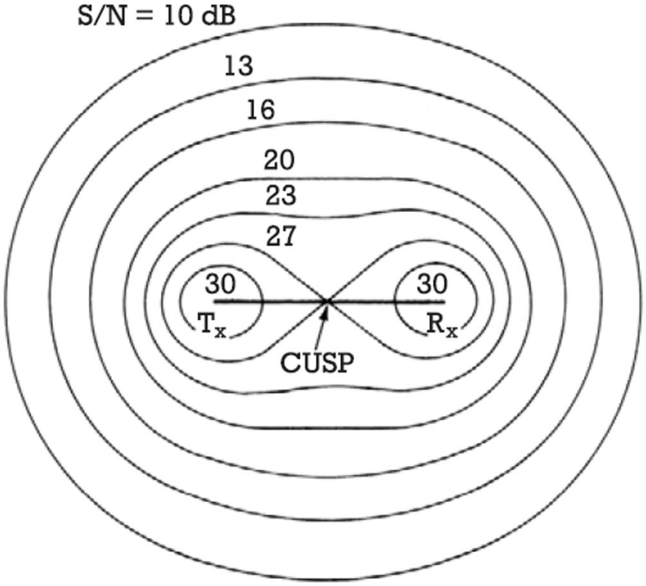

Starting from equation (1) for a given SNR, and solving for the range of the target (R_T), we can obtain this set of ellipses, which represent the possible locations of the object of interest based on the level of power received in the surveillance antenna in the simple case of a bistatic radar. In the case of multi-static radars, this set of ellipses intervenes with another group of ellipses, due to the other transmitter/receiver pair, enabling the triangulation that provides the exact position within an area of uncertainty.

Figure 5. The Ovals of Cassini. Source: [1].

B. SOURCES OF ILLUMINATION

Signals of opportunity comprise one of the essential parts of a passive radar, firstly because without those, we cannot have a passive radar, and then in a way that heavily affects the performance of the radar. Even though all signals theoretically can be used as signals of opportunity, some are more favorable than others. For any given area of interest, we may have several potential signals that may vary tremendously, while, on the other hand, there are areas, such as the polar regions that we investigate here, where we can experience a lack of such signals.

Usually, when we talk about signals of opportunity, we refer to anthropogenic signals from various sources. However, radio-astronomical sources such as the radio emissions from celestial bodies like the Sun and Jupiter have demonstrated promise as potential signals of opportunity for echo detection, as presented in various applications ([1], [2], [5], [8], [10], [14], [16]–[18]). Therefore, signals of opportunity can be divided into two main categories: artificial and natural. Table 1 presents the pros and cons of some of the different waveforms transmitted by systems that can be used as illuminators, where one can see the different perspectives of each type of illuminator with respect to applications on passive radar. GNSS signals provide global coverage, so they would be favorable for space-based applications of passive radars. On the other hand, sources such as FM (frequency modulation) radio and DAB (Digital Audio Broadcasting) provide high power level and good area coverage of urban areas.

Table 1. Overview of Advantages and Disadvantages of Signals of Opportunity. Source: [12].

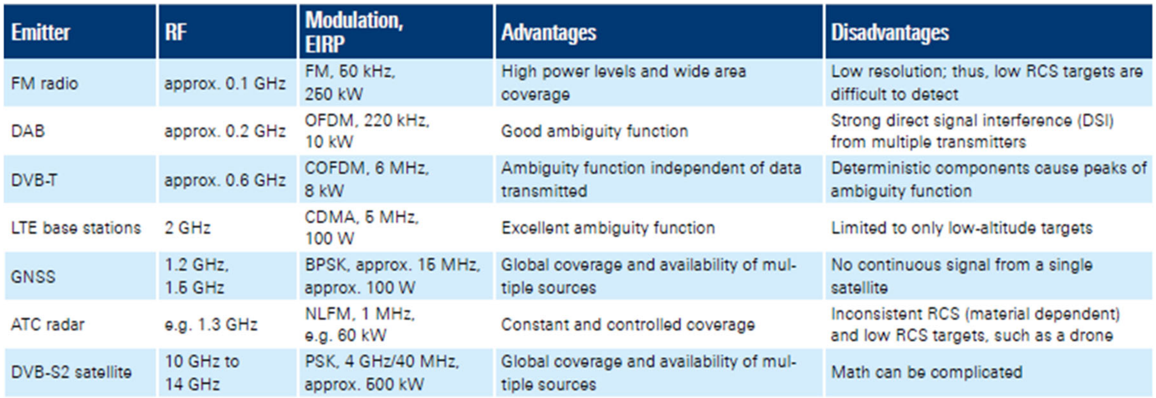

Emitter	RF	Modulation, EIRP	Advantages	Disadvantages
FM radio	approx. 0.1 GHz	FM, 50 kHz, 250 kW	High power levels and wide area coverage	Low resolution; thus, low RCS targets are difficult to detect
DAB	approx. 0.2 GHz	OFDM, 220 kHz, 10 kW	Good ambiguity function	Strong direct signal interference (DSI) from multiple transmitters
DVB-T	approx. 0.6 GHz	COFDM, 6 MHz, 8 kW	Ambiguity function independent of data transmitted	Deterministic components cause peaks of ambiguity function
LTE base stations	2 GHz	CDMA, 5 MHz, 100 W	Excellent ambiguity function	Limited to only low-altitude targets
GNSS	1.2 GHz, 1.5 GHz	BPSK, approx. 15 MHz, approx. 100 W	Global coverage and availability of multiple sources	No continuous signal from a single satellite
ATC radar	e.g. 1.3 GHz	NLFM, 1 MHz, e.g. 60 kW	Constant and controlled coverage	Inconsistent RCS (material dependent) and low RCS targets, such as a drone
DVB-S2 satellite	10 GHz to 14 GHz	PSK, 4 GHz/40 MHz, approx. 500 kW	Global coverage and availability of multiple sources	Math can be complicated

Note: Global coverage consists of the main advantage of signals that come from planetary missions, while FM radio and DAB signals provide high power levels and wide coverage in urban areas.

Figure 6 shows an overview of available illuminators divided into two categories, anthropogenic and natural. On the manmade side, sources of illumination are divided into two sub-categories, ground and space based, while on the natural side there are only two available sources, Sun's emissions and Jovian bursts, also known as Jovian radio emissions, which are primarily caused by the interaction of Jupiter's magnetosphere with its moon Io. Signals from existing satellite constellations in Low Earth Orbit (LEO), such as Iridium, Inmarsat, and the newer Starlink, and Telesat, represent another possible signal of opportunity for echo detection.

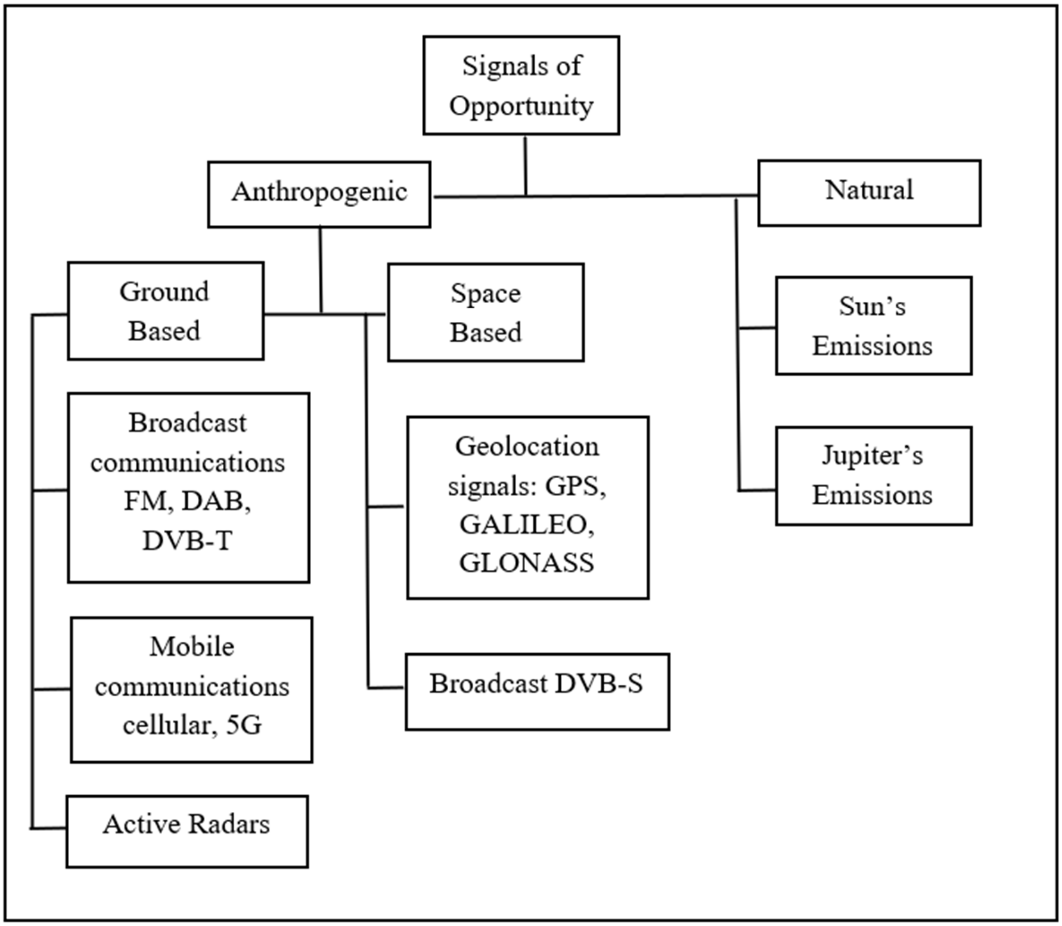

The available illuminators can be divided into two categories, anthropogenic and natural. Regarding artificial sources of illumination, they are categorized into ground-based and space-based sources. In the natural realm, there are only two sources: solar emissions from the Sun and Jovian bursts (or Jovian radio emissions). These bursts stem from the interaction between Jupiter's magnetosphere and its moon Io.

Figure 6. Signals of Opportunity. Adapted from [12].

C. OVERVIEW OF PASSIVE RADAR SOUNDING

This section focuses on how to optimize passive radar sounding measurements from a single channel passive radar when using a natural source of illumination, with the ultimate goal of measuring the height of an ice sheet. Although applications of passive radars are broad, there is little to no published research related to this topic.

Peters et al. [16] provided the first successful attempt to measure the thickness of ice sheets using passive radar [19]. Their article builds on the "sea-cliff Lloyd's Mirror experiment” [20], [21], which observed a gradually emerging pattern created by the interference of solar radio emissions [19]. It achieved this by transitioning to a rapid-time autocorrelation technique that avoids distance constraints. The passive radar was located on the peak of the ice sheet and received the Sun’s radiation both directly, and after reflection at the ice sheet’s base. The time difference between those two measurements, delay time Δt, was used to infer the ice sheet’s thickness. This new passive measurement technique of ice sheet thickness opens the door to other low-resource, passive, continuous observations such as keeping track of the melt rates, the amount of water stored inside the glacier, and rate of strain in the vertical direction ([2], [5], [8], [16]). Low-resource, passive, continuous observations can further assist in understanding how ice sheets react throughout a day or a year and, consequently, how they contribute to sea-level rise.

On this topic, another two articles by Peters et al. [8], [14] improved the SNR by 10 dB in both experimental and simulated data. In those cases, the estimation of the signal arriving directly at the receiver is performed by a deconvolution filter and then the algorithm uses CLEAN [22] processing for DSS (direct signal suppression).These papers demonstrated that emissions from the Sun and Jupiter, which are available in polar areas, can serve as ambient noise and would be preferable for passive radar measurements of glaciers, due to the fact that we have a prior knowledge of the position of the Sun and Jupiter and can predict their exact path [8].

Peters et al. [5] demonstrated the potential of using the Sun’s emissions for passive sounding. This article presents an approach that implements passive SAR using the Sun’s radio emission as ambient noise. In the first part of this research, the authors defined the critical SNR of echoes reflected off a rough surface and verified that the system can reliably observe the Sun’s echo reflection. Next, they described how to use passive radar to analyze the reflection of the Sun’s emission and detect changes in phase, range, and reflectivity [5]. Those changes are necessary to implement SAR. The experimental part of the research took place at Dante’s View, Death Valley, to verify that their technique could perform 2-D imaging. Then, after achieving a 2-D image of the floor of the desert, they also increased the SNR[5]. The results from the simulated data demonstrate that performing SAR passive imaging is possible by concentrating a planar white noise signal, improving the outcome

SNR, and angular accuracy [19]. The bottom line of this research highlights the feasibility of performing passive SAR using the Sun and Jupiter's radio emissions as ambient noise, highlighting the potential applications for surface and subsurface imaging for Earth or other planets. Finally, they emphasize that this kind of remote sensing would be favorable for continuous measurements of ice sheet thickness and other subsurface conditions at large scales, both on Earth and other bodies, like the icy moons of Jupiter.

Another publication on passive SAR by Peters et al. [9] presented a passive-sounding technique based on autocorrelation of the signals, aiming to map topography by taking advantage of the Sun's movement. It "demonstrates this technique's capability to measure the Sun's reflection off the rougher desert floor, which is more analogous to the bed of an ice sheet" [9]. Likewise, the goal of this work is to achieve passive SAR processing, observing changes in range, phase, and reflectivity over time and then constructing a 2D image from all the measurements as the Sun moves throughout the day. Succeeding in getting passive SAR measurements can assist in using this approach for measuring ice sheets with a low-resource asset.

Apart from the Sun's emissions, Jovian bursts are a valuable passive-sounding tool. For this reason, there are many studies based on these emissions. As Roberts et al. [10] state, measurement information, with only a receiver, regarding planetary and lunar surfaces and sub-surfaces, is feasible by passive sounding. Jupiter's magnetosphere can serve as a source of ambient noise with a highly structured spectral content that can enable passive sounding in the Jovian system and has potential applications on our moon. Nevertheless, as measurements by JUNO (Jupiter's Near polar Orbiter) indicate, the properties of Jovian bursts are not ideal white noise, which is not ideal and limits the performance of the passive radar. After analyzing 18 hours of burst data from the LWA1 (Long Wavelength Array 1) telescope from 2012 to 2017, and then using those data to create similar simulated signals, Roberts et al. discovered that signal characteristics included undesired broadening and echo-like behavior simulating the natural spectral variation. However, with a signal conditioning procedure, the authors suggest that high-quality corrections are feasible to mitigate these undesired effects.

Schroeder et al. [18] investigated if the installation of a passive radar on the two missions around Jupiter's icy moons by ESA and NASA, Radar for Icy Moon Exploration (RIME) and Radar for Europa Assessment and Sounding: Ocean to Near-surface (REASON), would be meaningful and add value to these missions by providing important information that the existing active radars do not offer or get better results than those of the active radars. Results indicate that in a noisy Jovian environment, the SNR might be even better than the equivalent of the active radar. At the same time, this is not the case in a quiet environment., Another field of research of this study was whether implementing a passive sounding in another frequency, within the band of decametric noise generated by Jupiter's radiation, would be beneficial. In conclusion, the authors suggest that a passive radar would add value to these missions as an additional channel, but a different frequency is unnecessary.

Another article, published by Gerekos et al. [23] before the RIME and REASON launch date, aimed to enlighten and optimize factors related to these missions. In this paper, Gerekos et al. suggest a technique to precisely replicate the reflections from the surface of a target of interest, in this case of a planetary body, such as Callisto, Ganymede, or Europa, for radar in active or passive mode, with external radiation being present. This technique is based on the Stratton-Chu simulator [24] and considers the main radar parameters potentially affecting the outcome. Gerekos et al. used two types of signals to perform this analysis: a white Gaussian noise (WGN) generated synthetically, and experimental waveforms taken from observations by the LWA1 mission. To estimate the performance of this model in a real task, radargrams from areas of Mars were created in both active and passive modes. Due to the lack of data from a real passive sounding mission, this part of the research was only validated by simulation.

In recent years, there has been an increased interest in the passive-sounding use of natural illumination sources. As more sophisticated algorithms become available, some of the flaws that passive-sounding sensors traditionally have, like low SNR, can be waived, making implementing these in future missions more appealing.

D. SOURCES OF ERROR

1. Direct Path Interference (DPI)

Direct Path Interference (DPI) or Direct Signal Interference (DSI) refers to the interference produced at the receiver by the direct signal. The part of the transmitted signal that arrives directly at the receiver without being reflected by a target or object of interest and the part that has been reflected and scattered by other surfaces, widely known as clutter, can be considered the direct signal. Figure 4 provides a good example that can assist in understanding the nature of the direct signal. In the more simplistic case, this signal arrives directly at the receiver without being reflected. In this case, it is much stronger than the reflected path. While the direct path is a reference signal, it can interfere with detecting the reflected signal. This part of the signal is always present in passive radars. It cannot be avoided because receivers use omnidirectional antennas, and the signals of opportunity are usually transmitted in all directions.

Recalling the geometry of passive radar, when the direct signal arrives at the receiver (surveillance antenna) without being reflected, its power is much greater than the equivalent signal that is received after being reflected off the target for two main reasons: (1) it travels less distance (the range between the source of illumination and the receiver antenna is called baseline [1]) and (2) it has less attenuation compared to the reflected signal. In other words, the power of the signal corresponding to the target is much weaker than the direct signal's power because it has scattered off the target and traveled a greater distance. Therefore, one possible way to increase the SNR of the radar is by removing, or suppressing, the part of the signal received from the surveillance channel that corresponds to the direct signal.

To extract the distance of a target from the location of the receiver, a passive radar measures the time difference of arrival between two signals: (1) the signal received directly by the reference antenna and (2) the transmission received at the surveillance antenna after being reflected off the target. The target distance can be estimated by applying auto- or cross-correlation techniques/filters between the signals received directly and indirectly. Auto-correlation techniques are used in the case of correlation between a time series and a lagged version of itself, helping identify patterns or dependencies within the same series over time. Cross-correlation, on the other hand, measures the correlation between two different signals, revealing how they relate to each other and whether one signal leads or lags the other. Nonetheless, the direct signal may unintentionally bleed into the surveillance channel antenna utilized for target detection. The resulting DSI must be reduced to a level that, in the ideal case, is below the receiver noise to avoid any reduction in the maximum possible detection range of a target of a given RCS. Therefore, the above concept explains why a direct path comprises one primary source of interference and needs to be removed or suppressed with DSS algorithms into a level below the receiver noise so a further decrease in the detection range is avoided.

The left panel of Figure 7 presents the concept of passive sounding translated in the way the antenna, indicated by the blue triangle, receives the two similar signals, the direct and the reflected, with the reflected being an attenuated and delayed replica of the original. Time delay (τ) is the time difference of arrival (TDOA) between the two signals, direct and reflected, that provides the desired information about the height of the icesheet. The top right panel of Figure 7 provides an example of how the received waveforms would appear from the direct and reflected paths, while the bottom right panel illustrates the combined plot of the two signals in time domain.

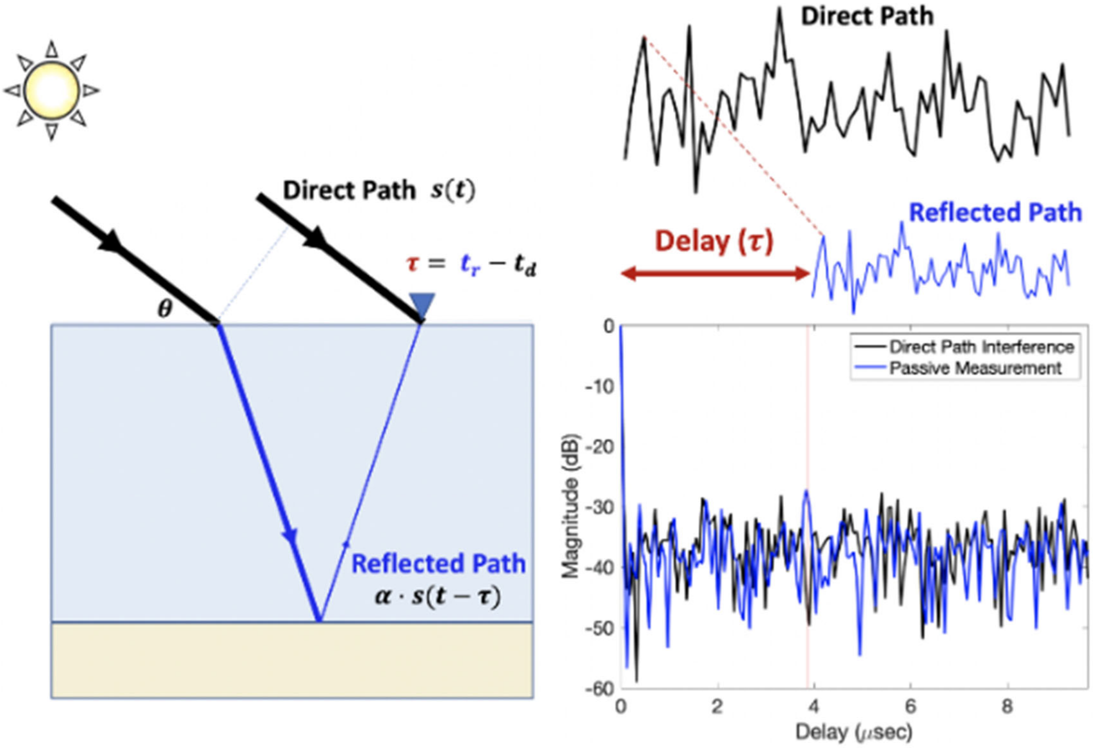

(Left) The blue triangle indicates the receiver of the passive radar, which receives first the Sun's emissions directly and then, after a time delay (τ) the signal that has been reflected at the bed of the icesheet. This time difference between those two similar signals in the autocorrelation provides us with the height, or thickness, of the ice sheet. (Right) The top panel provides an example of how the received waveforms would appear from the direct and reflected paths, while the bottom panel illustrates the combined plot of the two signals in time domain.

Figure 7. Time Delay between the Sun's Direct and Reflected Path. Source: [12].

2. Phase Errors due to Clutter

Clutter forms a source of interference that can limit the performance of the passive radar. Clutter consists of radar echoes generated by reflection from objects such as the terrain, sea, and things in the environment, like buildings and vegetation, other than the target, that co-exist with the environment of the target. However, clutter depends on the mission of each radar, as in the case of remote sensing synthetic aperture radars (SAR) where objects like terrain and sea are the primary targets of interest, an aircraft or a ship will create the unwanted clutter effects.

Although clutter can have similar effects in the outcoming SNR to those from the noise in the environment, clutter is different than noise. First, the amplitude of the clutter is potentially proportional to signal transmitted from the radar, while this is not true in the case of noise. Also, the bandwidth of the clutter is narrow, compared to the wide bandwidth of the noise. Clutter characteristics such as frequency and repetition patterns depend on the transmitted signal, while in the case of noise they are irrelevant of the transmitter.

Since clutter follows various paths before being received at the surveillance channel, which corresponds to different times of arrival at the receiver, each of those signals can introduce phase shifts, resulting in phase errors that distort the received radar signal and make it challenging to accurately determine the desired reflection that corresponds to the true range and location of the target. The problem of estimating and removing the clutter is like direct path interference removal, as this is another version of the original signal that has reduced intensity and was received with a small time difference [1], [25].

Regarding sounding from passive radars, reflections from the surface form surface clutter, which is a signal that has been delayed for the same time as the reflection from a given depth i.e., ice thickness. Therefore, the signal that corresponds to clutter can potentially mask the signal that corresponds to the target. One characteristic figure of performance is the signal-to-clutter ratio that measures the strength of the signal reflected on to base of the ice sheet, compared to the strength of the clutter [26]. Since the surface signal doesn’t undergo attenuation due to propagating through the ice sheet, it is generally significantly more intense than the nadir signal [27]. Furthermore, as described above, clutter depends on the source of illumination, therefore, clutter power tends to increase as sounding frequency increases, which does not affect as in the case of illumination from Sun or Jupiter. However, altitude also affects clutter, because increasing the height of an airplane or satellite results in decrease of the corresponding angle of arrival of the clutter signal, resulting in increased clutter power.

As Figure 8 presents, in the simplest case of a moving platform, without considering any roll of the sensor due to the movement of the platform, the surface clutter is a circular ring, whose size varied with varying duration of the pulse. Moreover, as depicted in Figure

8, in our case of measuring the ice thickness, the primary source of clutter is called firn clutter, and is generated by the granular snow on top of glacial ice, as the signal propagates through it to the base of the icesheet. The radar antenna receives several returns, represented by the various circle bins. Integration of all the returns form the clutter. The power recorded within a specific range bin results from the combination of backscatter originating from all dielectric interfaces.

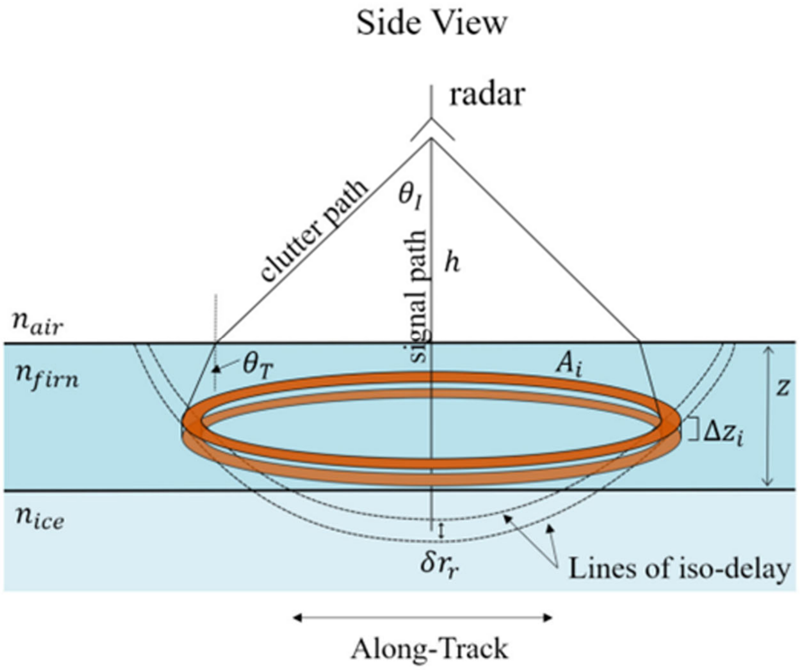

The main part of the clutter in passive sounding of icesheets is generated by the granular snow on top of glacial ice, as the signal propagates through it and is called firn clutter. The radar antenna receives a number of returns, represented by the various circle bins, that form the clutter. The power recorded within a specific range bin results from the combination of backscatter originating from all dielectric interfaces.

Figure 8. Clutter of Passive Radar Sounding for Icesheets. Source: [27].

3. Phase Errors due to Doppler Shift

A Doppler shift arises from changes in the received frequency of a wave because of the motion of both the source and the receiver relative to one another. The following cases describe the relative motion between the target and the receiver:

- A moving platform monitoring a stationary target,
- A stationary platform monitoring a moving target,
- A moving platform monitoring a moving target.

The phase change in the received signal due to the Doppler Shift is given by [28]:

$$\Delta\varphi = \frac{2\pi\Delta l}{\lambda} = \frac{2\pi v\Delta t}{\lambda} \cdot \cos\alpha \tag{2}$$

where $\Delta\varphi$ is the phase difference that corresponds to the time difference of Δt, α is the angle between the direction of motion and the signal response after being reflected to the target, and v is the relative velocity.

Figure 9 presents the case where a satellite is initially moving towards the target of interest, resulting in an increased number of pulses received from the receiver mounted on the satellite. In this case, f_d will be positive, resulting in the received frequency being greater than the original frequency of the signal of illumination. Then, when above the target, f_d will be zero, making the frequency of the received signal equal to the original frequency. Finally, when the satellite recedes, the received signals are less than those transmitted by the illumination source, resulting in negative f_d, that corresponds to received frequencies lower than the original frequency. Doppler frequencies f_d depend on the relative velocity between the radar and the target, which in our case reduces is the speed of the satellite, as the target is stationary.

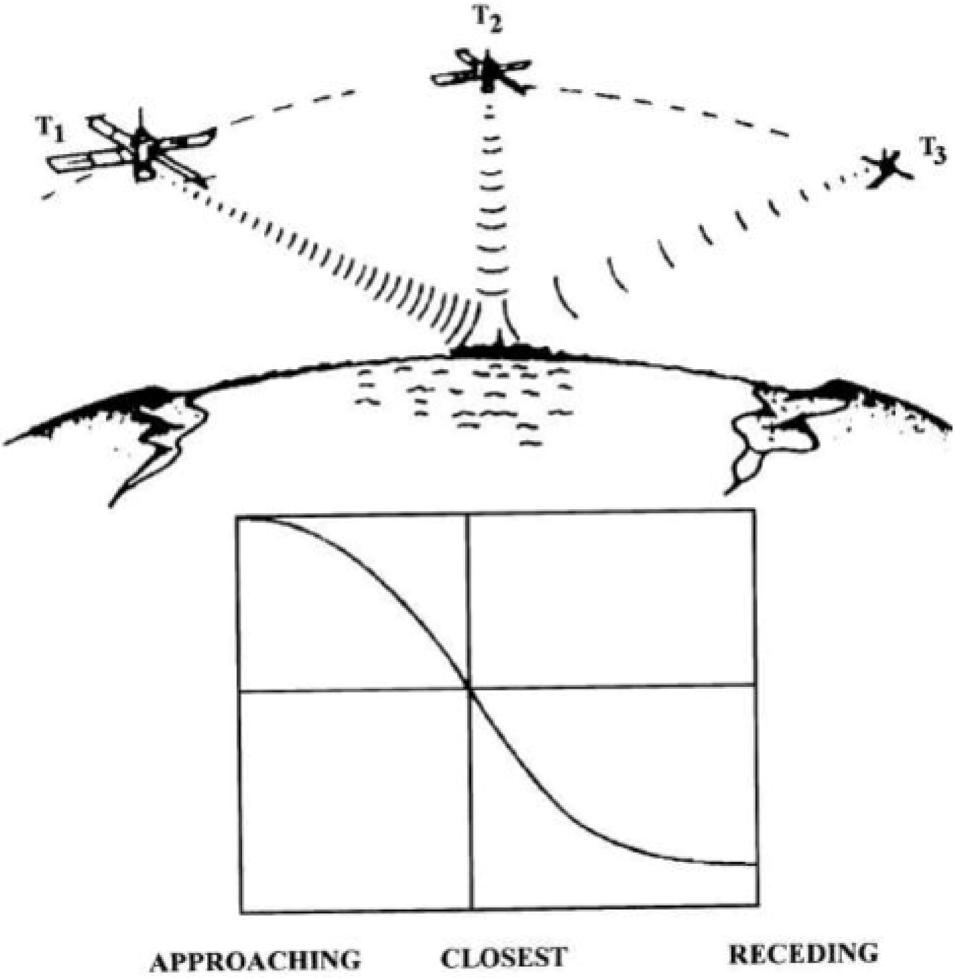

An example of monitoring a stationary target from a moving platform is a radar on a satellite, which generates a Doppler shift. This change in frequency increases as the satellite approaches the target and decreases as the satellite recedes.

Figure 9. Example of Doppler Shift. Source: [29].

The Doppler shift corresponding to the case described above and depicted in Figure 9 [28] is represented by

$$f_d = \frac{1}{2\pi} \cdot \frac{\Delta\varphi}{\Delta t} = \frac{v}{\lambda} \cdot \cos\alpha = \frac{f_c v}{c} \cdot \cos a \tag{3}$$

where f_c is the original frequency of the electromagnetic wave and c is the speed of light in free space. Doppler shift and the phase errors generated from it are a topic of investigation in this research, as we are interested in how the outcome of SNR is affected by those phase errors.

4. Phase Errors due to the Ionosphere

Earth's ionosphere, as every planetary ionosphere, affects the propagation of electromagnetic waves. Due to the significance of the effects of the ionosphere in the propagation of signals and the potential phase shifts that are generated, many studies exist, not only for Earth's ionosphere, but for other planet that have ionosphere, such as Mars and Jupiter's moon, Europa.

The ionosphere is the upper part of Earth's atmosphere, where a layer of electrons is created due to the ionization of atoms and molecules by specific wavelengths of solar radiation. In this region, the plasma is populated with an equal number of positive and negative charges, rendering it electrically neutral. Within this environment, electrons and ions co-exist with various neutral particles. The interaction between electromagnetic waves and the charged particles of the ionosphere produces a highly dispersive media, which depends on the electrons concentration and the polarization of the plasma. Electrons and ions oscillate within this region at the plasma frequency (f_p), which depends on the density of the plasma (N_i). Because electrons are much lighter than ions, on the order of 1,000 – 10,000 times, they are the main contributor in the plasma oscillations. The plasma frequency is given by [30]

$$f_p = \frac{q_i}{2\pi\sqrt{\varepsilon_0 m_i}}\sqrt{N_i} \tag{4}$$

where

f_p is the plasma frequency (Hz),

ε_0 is the permittivity of free space ($8.854\text{x}10^{-12}$ F/m),

q_i is the charge of the particle (Coulombs),

m_i is the mass of the particle (kg),

and N_i is the particle density.

Equation (4) reduces to

$$f_p = 8.98\sqrt{N_e} \tag{5}$$

where fp is the plasma frequency (Hz) and N_e is the electron density (electrons per cubic meter), if we substitute the values of mass and charge that corresponds to electrons, as ions do not play a significant role in the plasma oscillation.

Propagation through ionosphere generates a dispersive phase shift (Δφ), where different frequencies within a wave propagate with different speeds within the medium. When a wave contains multiple frequency components, each frequency can experience a different phase shift as it propagates. The phase shift for a 2-way propagation of the wave through the medium is given by [30], [31]

$$\Delta\Phi_{2-way} = -\frac{4\pi f}{c}\int_0^h real(n-1)dz \tag{6}$$

where

n is the refractive index of the plasma,

c is the speed of light in vacuum (m/s),

and f is the frequency of the signal (Hz).

The refractive index of the plasma, in the case that gyrofrequency is much smaller than plasma frequency, is given by [30], [31]

$$n^2 = 1 - \frac{2\pi f_p^2}{2\pi f^2 - ifv} \tag{7}$$

where v represents the phase velocity. Assuming that phase velocity is negligible compared to the frequency of the wave and then applying a first order approximation to the refractive index formula we obtain [30], [31]

$$n = 1 - \frac{f_p^2}{2f^2}. \quad (8)$$

Then, by substituting equations (5) and (8) into equation (6) we obtain [30], [31]

$$\Delta\Phi_{2-way} = \frac{q_e^2}{2\pi\varepsilon_0 m_e c f} \int_0^h N_e(z)dz. \quad (9)$$

Next, substituting the constants we get [30], [31]

$$\Delta\Phi_{2-way} \approx \frac{1.69 \cdot 10^{-6}}{f} \cdot TEC \quad (10)$$

which is only dependent on the frequency of the transmitted signal and the TEC of the ionosphere. TEC, which actually refers to VTEC (Vertical Total Electron Content), is the result of integration of electron density (N_e) from the surface of the earth to the desired height (h), presented at equation (9). One popular method to estimate TEC for Earth's ionosphere is by measuring the time delay between two signals with different frequencies [31].

E. DIRECT SIGNAL SUPPRESSION

As stated previously, while the direct path serves as a reference signal, it also interferes with detecting the reflected signal, explaining why it needs to be removed or suppressed from the surveillance channel. This can be achieved in several ways, divided into two main categories: analog and digital techniques. However, research on this topic indicates that to be more flexible and employ more channels and different geometries, digital strategies, especially adaptive filtering, are preferred [32]. A brief overview of these options is provided, with an extensive reference to one that will be investigated in this work.

Analog techniques

- Physical shielding: This approach employs physical obstacles, such as radar fences, buildings, or radar absorbent materials (RAM), that can be placed between the receiver and the transmitter (source of illumination) to decrease the effect of direct path into the surveillance antenna.

- Adaptive antenna nulling: Adaptive beamforming can create a null surveillance channel in the transmitter's direction. For a fully digital antenna, adaptive beamforming provides a means to reduce sensitivity in alignment with the source of the directly received signal. When external factors like multipath-induced noise are introduced, the formation of multiple nulls might be necessary.
- Hardware cancellation: This method employs specialized hardware components designed to actively suppress or subtract the direct signal from the received signals. By implementing hardware cancellation, unwanted direct signals can be significantly attenuated.

The techniques discussed, although they can achieve the primary goal of suppressing direct signal, usually result in:

- Limited flexibility in the design process, significantly if the locations of the sources of illumination or the substantial interference is changing.
- Decreased detection levels in the transmitter's direction or other strong interferences that must be nulled.

Digital techniques:

- Fourier processing: Since most illumination sources are stationary, the signal corresponding to the direct path and the multipath will not have a Doppler component, or their Doppler component will be known and predictable based on the platform's movement [1]. This makes it easier to identify leakage of the illumination source into the surveillance channel as compared to the Doppler shift of a return from a moving target. However, this approach is less useful for slow-moving targets without a large Doppler shift.
- Adaptive filtering: This approach improves the SNR by estimating and removing the incoming direct signal from the surveillance channel. To do so,

the incoming signal in the reference channel is sampled in an interval T_s, such that $t = nT_s$, where n represents the number of samples [33]. Then, this passes through an impulse response filter [32], constructing the signal received in the surveillance antenna, consisting of the estimated direct path, clutter, and multipath components. The reference signal, s_r, propagates via the channel illustrating the direct path and clutter components [33]

$$s_{DSI}(n) = \sum_{i=0}^{M-1} h^*(i)\, s_r(n-i) \tag{11}$$

where s_{SDI} represents the estimation of the interference due to the direct path size, s_r is the reference signal, M is the length of significant coefficients and h(i) is the impulse response function. DSI suppression aims to remove the direct path signal from the surveillance channel.

The steps for DSI removal are:

(1) Estimate of the clutter and direct signal components that currently are not known,

(2) Compare the result to the signal received at the reference channel,

(3) Estimate direct signal $s_{SDI}(n)$,

(4) Remove this result from $s_s(n)$,

(5) $s_c(n)$ is the new clean signal, free of $s_{SDI}(n)$. The mathematical representation of this is given by [33]

$$s_c(n) = s_{DSI}(n) + s_{tar}(n) + v(n) \tag{12}$$

where $s_c(n)$ is the signal clean of interference, $s_{SDI}(n)$ represents the estimation of the interference due to the direct path, $s_{tar}(n)$ the signal that corresponds to the reflection of the target and *v(n)* is the additive noise.

A typical example of the processing flow of a general model for an adaptive filter is given in Figure 10, where the reference and surveillance channels are represented. The flow the signal starts at the top left corner of the figure, where the signal is received by the radar with both the antennas, surveillance, and reference. The goal of the filter is the approximation of the waveform of the direct signal, illustrating the adaptive character of the algorithm. The signal received by the surveillance channel, represented by the right block, includes the interference due to the direct path s_{SDI}(n), the signal that corresponds to the reflection of the target s_{tar}(n) and the additive noise *v(n)*. Finally, after comparing the signals that come from the two different channels, the direct path is removed from the signal of the surveillance channel, which then creates the clean signal s_c(n).

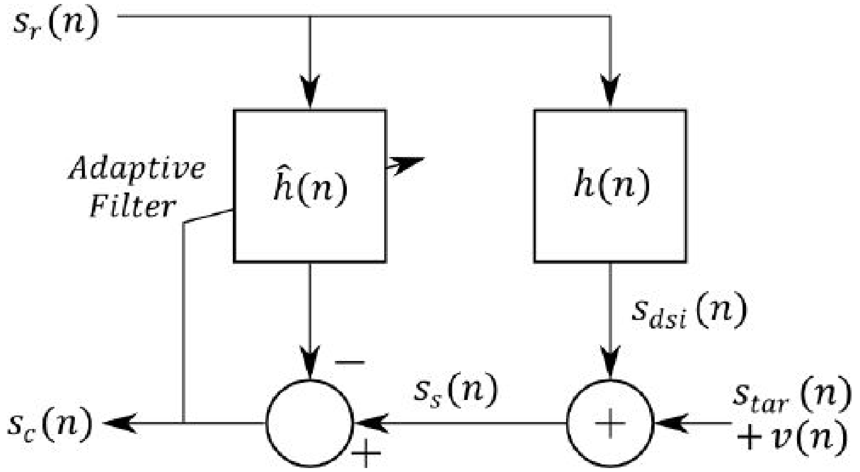

The signal flow commences from the top left corner of the diagram, where the surveillance and reference antennas capture the signal. The left square block represents the reference channel, whose objective is to constantly refine the estimation of the direct signal waveform, demonstrating the adaptive nature of the algorithm. In the surveillance channel, represented by the right block, the received signal incorporates interference from the direct path (s_{SDI}), the signal corresponding to the reflection of the target s_{tar}, and additional noise (v(n)). Subsequently, by comparing signals from the two distinct channels, the direct path is eliminated from the surveillance channel's signal, resulting in the generation of a clear signal, s_c(n).

Figure 10. Block Diagram for Suppression of the Direct Path. Source: [33].

Since removing direct path interference is essential for making passive measurements feasible, there has been much research into signal-processing techniques that perform this process. The two main categories of DSI suppression are non-varying (fixed) coefficient and adaptive filtering. The first method assumes that the interference components are static throughout the "coherent processing interval" (CPI) [32], although this is not usually the case because clutter is not constant over time, and there are other instabilities that may occur. On the other hand, adaptive filtering automatically employs time-varying signal statistics, which usually leads to more accurate results, but can also degrade the result if not applied properly. Adaptive filtering techniques can be further divided into block and fully adaptive schemes, depending on how they update the filter coefficients $\hat{h}(n)$. The main difference is that in the first category, block schemes, filter coefficients $\hat{h}(n)$ are updated in a specific frequency (after a specific number of samples), while in fully adaptive category the filter coefficients are updated in every sample [32]. An overview of the existing signal processing techniques is presented as follows:

Adaptive filtering techniques

- Recursive Least Squares (**RLS**): RLS is a method that iteratively seeks the coefficients that reduce the "weighted linear least squares cost function" associated with the received signal. This algorithm aims to minimize the total squared variances between the signal reflected by the target signal and the filter's output, by comparing the new incoming signals, with the coefficients of the filter being updated at each iteration. RLS algorithms are known for their outstanding performance with the trade-off of increased computational demands[1], [32], [34].
- Normalized Least Mean Squares (**NLMS**): Normalized LMS is an extension of one of the most popular adaptive algorithms, LMS. It updates filter coefficients proportionally to the gradient of the mean squared error, allowing it to adapt to changing environments. Moreover, NLMS aims to overcome one of the main drawbacks of the original algorithm, its convergence speed, that made it not useful in many real scenarios, by normalizing the input by its power [1], [32].
- Fast Block Least Mean Squares (**FBLMS**): FBLMS is another variation of LMS algorithm, such as NLMS, designed to operate efficiently on large datasets or in situations where computational resources are limited.

The main difference between FBLMS and LMS is that it updates the filter coefficient not for every sample but for a block of samples. This change makes FBLMS faster and more computationally efficient, compared to LMS, resulting in being preferred in the cases of real-time applications or computational power is limited [1], [32], [35].

<u>Fixed coefficient techniques</u>

- Least Squares (**LS**) or **Wiener Filtering**: This method generates an estimate of the original signal by linear time-invariant (LTI) filtering of the received signal which contains the direct and reflected path and the noise. It minimizes the sum of squared differences between observed and predicted values to find the best-fitting parameters. Then, after filtering all the undesired variables from the received signal, the algorithm provides an estimation of the signal of interest [1], [32], [36].
- Extensive Cancellation Algorithm (**ECA**): The ECA algorithm is employed to eliminate unwanted direct path leakage from the overall signal. It achieves this by subtracting copies of the signal received in the reference channel that have the right amplitude and time delay from the surveillance signal. The actual delay of the signals is weighted according to adaptively coefficients, which are estimated by taking the average of the entire coherent processing interval (CPI) [1], [32], [37].
- **CLEAN**: This algorithm has applications in many scientific fields. However, it is broadly used in image recovery techniques, in radio astronomy, to restore any distortions due to the instrument or other undesired disturbances. Furthermore, CLEAN is a deconvolution algorithm which subtracts point sources from the image [1], [32], [38].

Due to the importance of decreasing the negative effects of the direct path signal, there has been an increase in investigation for the results of DSS algorithms in recent years. Numerous research efforts have tested available methods and compared their results. Extensive work in testing these algorithms and implementing the results of the comparison has been performed by Garry et al. in [32] and [33]. The increased demand for algorithms that suppress the direct channel explains the development of various techniques that were described above. A summary of the main existing DSS algorithms, is presented in Table 2. Each of these algorithms has pros and cons, depending on the application. Finally, there may be other algorithms as well, which can be variations of these algorithms or not, that suppress the direct signal.

Table 2. Summary of Digital Techniques for Direct Signal Suppression

Direct Signal Suppression – DSS	
Digital Suppression Techniques	
Adaptive filtering	**Fixed Coefficient**
Recursive Least Squares (**RLS**)	Least Squares (**LS**) or **Wiener Filtering**
Normalized Least Mean Squares (**NLMS**)	Extensive Cancellation Algorithm (**ECA**)
Fast Block Least Mean Squares (**FBLMS**)	**CLEAN**

THIS PAGE INTENTIONALLY LEFT BLANK

III. DIRECT SIGNAL SUPPRESSION FOR A SINGLE CHANNEL PASSIVE RADAR

A. INTRODUCTION

This chapter expands upon previous work performed by Peters et al. [14], simulating a single-channel, ground-based, stationary passive radar that uses the Sun's emissions as a source of opportunity to measure the thickness of ice sheets in a remote area like polar regions. Two critical parameters, the estimated echo peak power (α) and delay time (τ), which are used to construct the impulse response function, affect the SNR of the radar. The construction of the impulse response function is part of the signal processing algorithm that removes the direct path from the received signal. These results were presented at the international IEEE (Institute of Electrical and Electronics Engineers) conference regarding remote sensing, IGARSS 2023 (International Geoscience and Remote Sensing Symposium), in Pasadena, California, in July 2023 [2].

One of the drawbacks of passive radars is that they suffer from low SNR. Most of the time, applications of passive radars depend on advanced signal processing techniques to improve the resulting SNR. As seen in the previous chapter, one effective way to increase the SNR is to suppress the direct path interference. Traditional techniques that remove DPI require both reference and surveillance channels. However, removing DPI with just a single-channel radar would reduce the number of hardware components, logistical complexity, and power requirements of the radar [14]. This chapter investigates the role of α and τ in the impulse response function of the algorithm and how different values affect SNR.

Figure 11 presents the setup of the problem; a single-channel passive radar (labeled RX in the figure) sits on top of an ice sheet, receiving emissions directly from the Sun and after reflection from the bottom of the ice sheet. Measuring the time difference between those two similar signals provides an estimate of the height, or thickness, of the ice sheet.

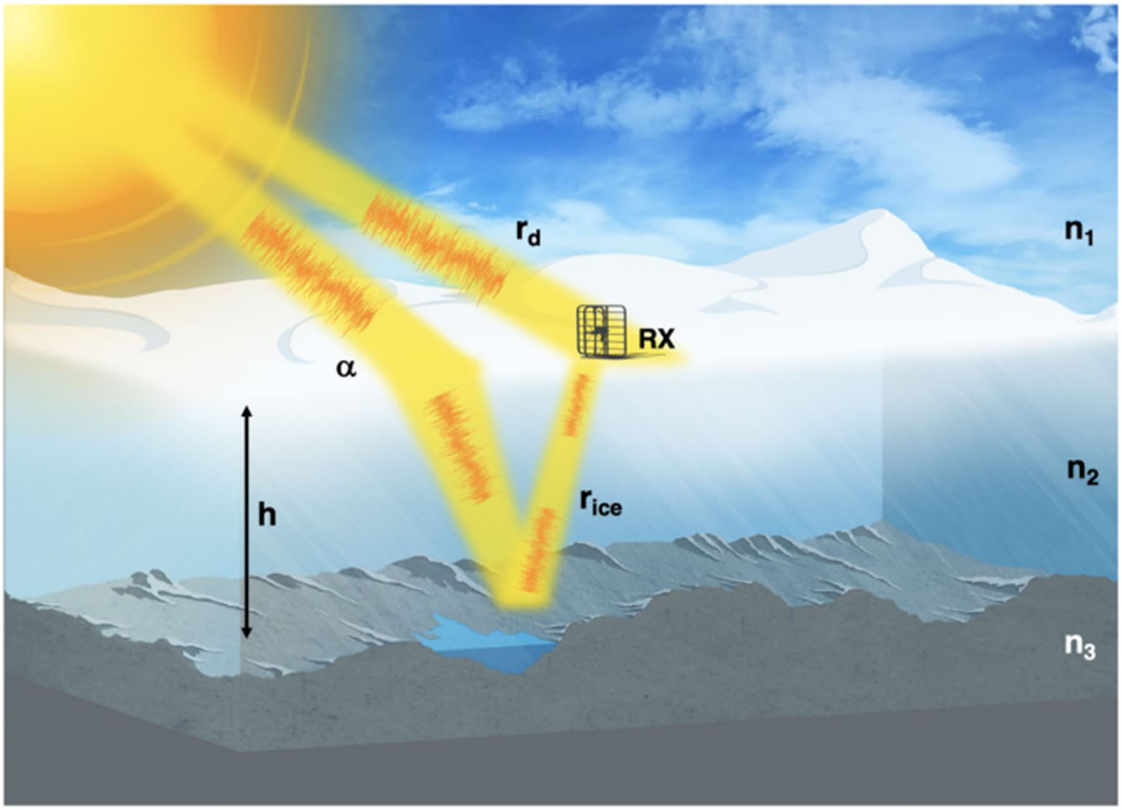

The single channel antenna sits on the top of the ice sheet, receiving emissions directly from the Sun and, after reflection, at the bottom of the ice sheet. Reference and surveillance channels are both in the same antenna.

Figure 11. A Passive Radio-Sounding Approach. Source: [8].

Essential assumptions of this problem are:

- The Sun is far enough from Earth that the received waves are parallel.
- The integration time is small enough so the position of the Sun can be considered stationary.
- The Sun's position is known a priori.

B. METHODOLOGY

In this part of the thesis, we describe and expand on the methodology used in the simulations.

1. Adaptive Direct Signal Suppression for Single Channel Passive Radar Sounding

In the ideal case, the three components of the signal that arrive at the receiver of a passive radar system are [2], [14] 1) the direct path (natural or artificial) $s(t)$, 2) an attenuated and delayed version of the direct signal $\alpha \cdot s(t-\tau)$, which stands for the echo of the original signal off a target, and lastly, 3) the noise of the environment $n(t)$. The three components of the signal that arrive at the receiver of a passive radar system can be represented mathematically by [2], [14],

$$x(t)=s(t)+\alpha \cdot s(t-\tau)+n(t) \tag{13}$$

where one can see the dependence of the observed signal on the peak power of the reflection, which contains the attenuation due to following a different and longer path and the delay time. Attenuation due to scattering, propagation in a longer and denser medium than the direct path, and reflection at the ice sheet's base affects the echo peak power coefficient.

Since the direct signal is much stronger than the attenuated and delayed parts, removing it will improve the resulting autocorrelation. Since there is not a dedicated reference channel to estimate the direct path, we construct the Wiener filter, *V(f),* in the frequency domain as [14]

$$V(f)=\frac{H^*(f)S(f)}{|H(f)|^2 S(f)+N(f)} \tag{14}$$

where S(f) corresponds to the mean power spectral density (PSD) of the signal received directly, N(f) corresponds to the PSD of the noise component n(t), H(f) corresponds to the impulse response function in the frequency domain of a linear time-invariant system (LTI), H*(f) corresponds to its complex conjugate, and f represents the frequency of the signal in Hz.

The polar and planetary regions of interest are generally considered environments with low noise components, transforming the previous relationship about the Wiener filter into

$$V(f) = \frac{H^*(f)\cancel{S(f)}}{|H(f)|^2\,\cancel{S(f)} + \cancel{N(f)}} \Rightarrow V(f) = \frac{1}{H(f)} \tag{15}$$

The mathematical formula of the impulse response function, in the time and frequency domain, are given by [2]:

$$h(t) = \delta(t) + \alpha \cdot \delta(t - \tau) \tag{16}$$

and

$$\mathrm{H}(f) = 1 + \alpha \cdot e^{-j2\pi f\tau} \tag{17}$$

respectively.

As one can see from equations (16) and (17), the two critical parameters of the impulse response function are the echo peak power (α) and the time delay (τ). As we do not have a dedicated channel to compute the exact values of these parameters, we aim to estimate those values as accurately as possible because an incorrect estimate will negatively impact the SNR of the radar. Also, since many parameters, such as ambient noise intensity, incident angle, sensor-target geometry, or ice sheet height, can change the constructed Wiener filter should be recalculated every time.

It is crucial to note that prior knowledge of the peak power and the delay time of the reflection are required. There are several ways to compute the values of those parameters:

- Estimate α and τ. The Sun's position is known and the relative power can be extracted from the first autocorrelation between the two different peak powers [5], [14].

- Ice sheet models can provide a fair approximation of α and τ.
- Use an ice-penetrating active radar to make the initial measurements.

Figure 12 depicts the concept of the signal processing flow used in this research, with a goal of removing the undesired direct path component from the radar receiver (presented by Peters et al. [14]).

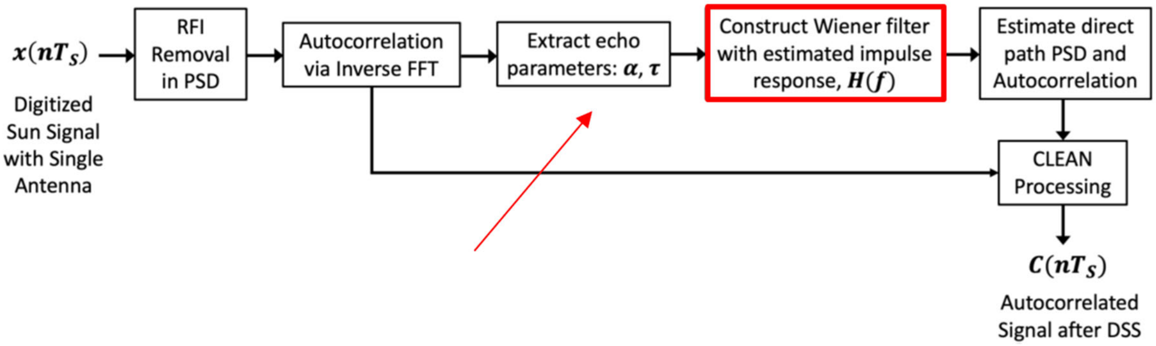

In this thesis, we will investigate how the estimation of values for echo peak power, α, and delay time, τ, when input to the Wiener filter affect the performance of the radar, aiming to optimize it to take the best SNR possible. Therefore, the part of the algorithm that we will investigate is presented in red color.

Figure 12. Signal Processing Flow of the Single Channel Passive Radar. Source: [14].

2. Optimization of Direct Signal Suppression Algorithm

Constructing the optimal Wiener filter by accurately estimating α and τ will lead to optimization of the algorithm, represented mathematically by [2]

$$\begin{aligned} &\max |\mathcal{G}(\alpha,\tau)|^2 \\ &w.r.t.\ \alpha,\tau \\ &subject\ to\ \ \tau > 0 \\ &\qquad\qquad\quad 0 \le \alpha \le 1 \end{aligned} \tag{18}$$

where $G(\alpha,\tau)$ is the SNR, α is the echo peak power of the received signal and τ is the time delay. The optimization of the algorithm improves the SNR, which then can lead to other advantages, such as capability of measuring higher icesheets or performing measurements from more distant orbits. However, the optimization of the performance of the radar takes place with respect to α and τ. The first restriction illustrates the zero-time signal reception, which corresponds to the direct path, and should be excluded. The second restriction illustrates the boundaries for the values of α, as it represents the amplitude of the signal, that fluctuates from 0 to 1.

0 presents the parameters used in the synthetic data simulation for this project. The DSS algorithm was applied to simulate white noise to echo autocorrelations data in MATLAB, representing a ground-based, stationary, passive-sounding system. The first seven parameters listed in the table were used by Peters et.al. in [14], and were kept constant in this work in order to be consistent. Values of the flux density of the Sun's signal and the background noise are presented, as well as the center frequency, the bandwidth, and the integration time of the hypothetical receiver. The height of the icesheet and Sun's angle form the hypothesis of the problem, as set by Peters et.al. [14]. Finally, we ran 10,000 simulations due to the gaussian character of the incoming signal, both emissions of the Sun and the galactic noise. To get more reliable results we needed to have an increased number of repetitions in the algorithm. The expected time delay was set to the actual delay corresponding to the height of the icesheet. Knowing the actual thickness of an icesheet is potentially a valid assumption, as there are various tools such as ice penetrating active radars and ice sheets models that can assist in predicting the height of icesheets. Therefore, we started from the actual time delay and searched around this value to understand how a small error in our estimation can affect the SNR of the radar. The same assumption was made for the power of the echo α, which corresponds to an amplitude of -10dB. To get a reliable result from our simulations and understand how SNR fluctuates, we searched in a region of 100 values around the actual values of α and τ.

C. RESULTS

1. SNR with Respect to Estimated Time Delay Used to Construct the Wiener Deconvolution Filter

In the first part of the simulations, we started by changing the time-delay around the expected value and then calculating the SNR. Figure 13 presents the results of 10,000 autocorrelations of synthetic data, altering the time delay value used in the Wiener filter by ± 5 times the sample period around the optimum value of 3.45 μsec. This is the estimated value of time delay that is used to estimate the direct path. In this figure, there is one main lobe with a strong peak of 26.12 dB, representing the actual time delay of 3.45 μsec, which corresponds to the case that the estimation of the direct path is the optimum, and provides the best SNR for this problem's setup. Apart from the main lobe, there are nulls, and sidelobes that create a decaying 'sinc' function pattern; away from the optimum time delay, the SNR decreases. The red, dashed line illustrates the -3dB margin, which is a common figure of merit indicating reception of half power, while the blue, dashed line illustrates the actual time delay.

Table 3. Simulation Parameters. Adapted from [2], [14].

DSS Optimization Simulation Parameters	
Description	**Specification**
Sun's Signal Flux Density	$4\text{x}10^{-14}$ [W Hz $^{-1}$m^{-2}]
Galactic Background Noise Flux Density	$1.4\text{x}10^{-14}$ [W Hz $^{-1}$m^{-2}]
Center Frequency	330 [MHz]
Receiver Bandwidth	15.36 [MHz]
Passive Integration Time	100 [μs]
Height of ice sheet	2000 [m]
Sun's angle	15[°]
Number of Simulations	**10,000**
Expected Delay Time (τ)	**3.45 [μs]**
Expected Echo Peak Power (α)	**-10dB**
Number of search values of τ	**100**
Number of search values of α	**100**

Note: Simulation parameters used at the synthetic data of white noise echo autocorrelations for a ground-based, stationary, passive-sounding system.

One important takeaway from Figure 13 is the strong dependence of the SNR on the estimated τ, and how the calculated SNR decreases if the value of τ used in the Wiener filter is not accurate. Furthermore, in the case of estimating τ out of the boundaries of the main lobe, the expected SNR will be significantly lower than the expected, which can be used as an alert to recalculate and adapt our values in the Wiener filter.

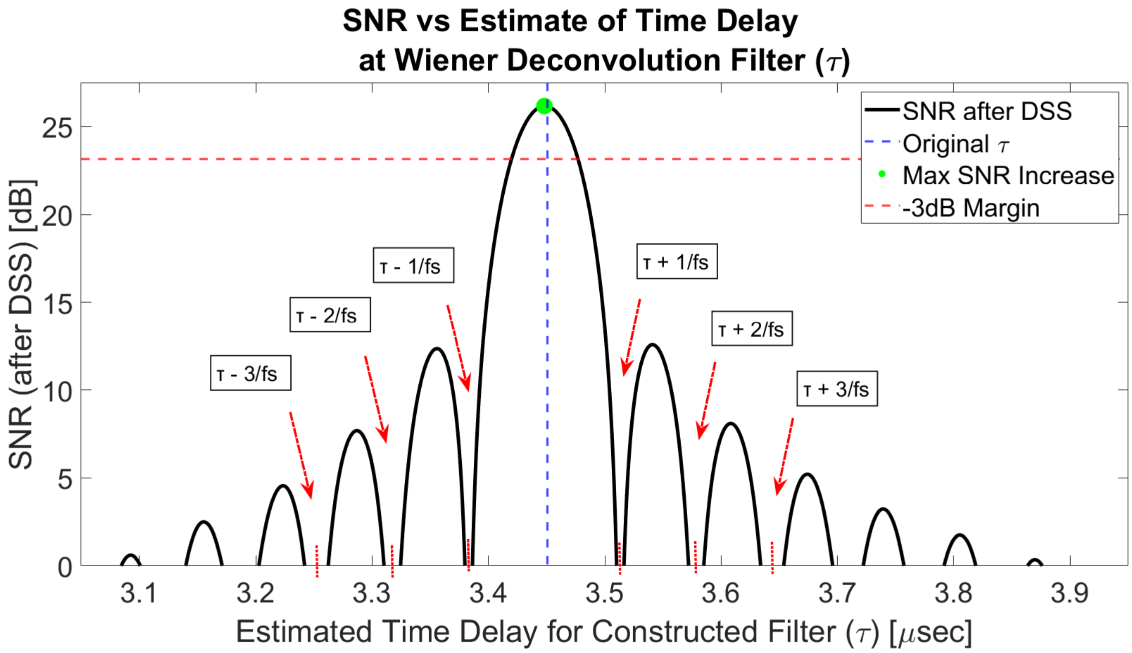

SNR vs. a varying estimated time delay (τ) at the Wiener deconvolution filter of ± 5 times the sample period around the optimum value of 3.45 µsec, based on results of 10,000 autocorrelations of synthetic data. The red, dashed line illustrates the -3dB margin, which is a common figure of merit indicating reception of half power, while the blue, dashed line illustrates the actual time delay. Red arrows point out the nulls that introduce the sidelobes of reduced power, creating an overall look of a decaying signal.

Figure 13. Dependence of SNR on Delay Time (τ). Source: [2].

Figure 14 is a zoomed-in version of Figure 13, around the optimal time delay value of 3.45 µsec, depicting the main lobe with the strong peak of 26.12dB. The key takeaway from this figure is that only slight deviations from the estimated value for τ, on the order of 0.06 µsec, are enough to generate a significant decrease in radar performance. A departure from 3.45 µsec on the order of 50% will decrease the SNR by 3dB, presented by the red, dashed line, compared to applying the optimal filter. As in the previous figure, the blue, dashed line indicates the actual time delay of the signal.

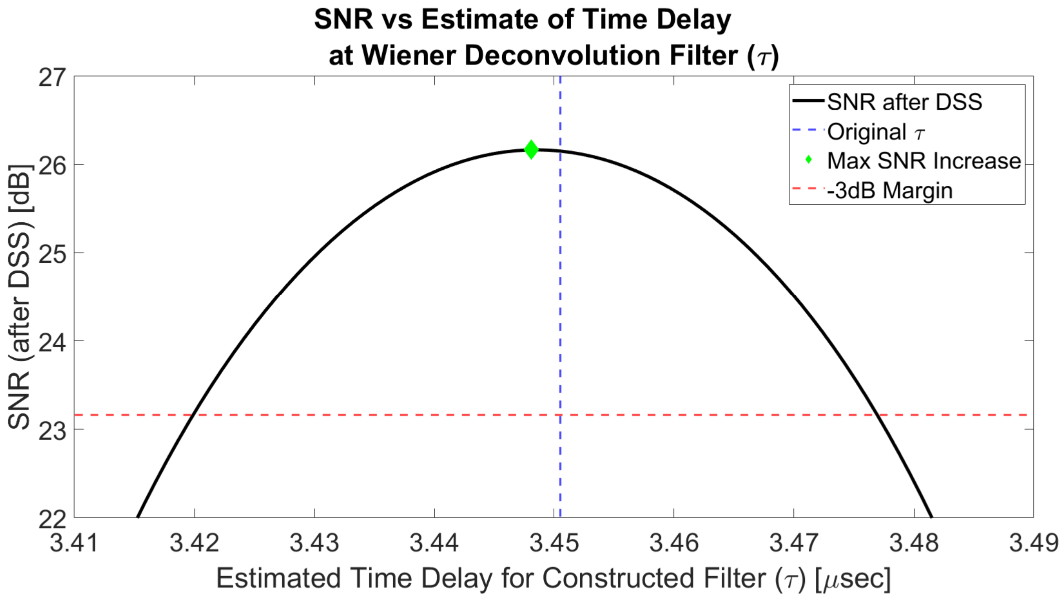

Results of 10,000 autocorrelations of synthetic data, altering the value of the delay time τ, that we input to the Wiener filter, only 50% around the optimum value of 3.45 μsec. The red, dashed line illustrates the -3dB margin, which is a common figure of merit indicating reception of half power, while the blue, dashed line illustrates the actual time delay.

Figure 14. Zoomed in Version of Dependence of SNR in Delay time (τ). Source: [2].

2. SNR concerning Echo Peak Power and Time Delay Used to Construct Wiener Filter

As can be seen by equations (16) and (17), apart from the time delay, the second parameter affecting the SNR of the radar is the value of the estimated echo peak power (α) fed into the Wiener filter. The values of α can vary from 0 to 1, with the estimated value for this problem being around 0.1, or -10 dB. Figure 15 depicts how increase in SNR from the original value of SNR, without implementing the DSS algorithm, is affected by these two variables, α and τ, when they vary around their optimum values. As in the previous section, the simulation took place 10,000 times to minimize the effects of the WGN of Sun’s emissions and galactic noise. As opposed to what was found when investigating τ, in the case of α even significant deviations of α produce only small decreases in the SNR of the radar, on the order of 1 dB. This can be seen from the yellow ellipse, which corresponds to 12.5 dB, just 0.51 less than the optimum SNR increase, even for a large difference in the values of the estimated α. On the other hand, the dependence of SNR on the value of estimated τ is important, as deviations of ± 0.03 μsec significantly reduce the increase of SNR. Finally, the star indicates the case when optimum estimation of both τ and α is achieved, which would provide the best possible SNR increase of 13.01 dB.

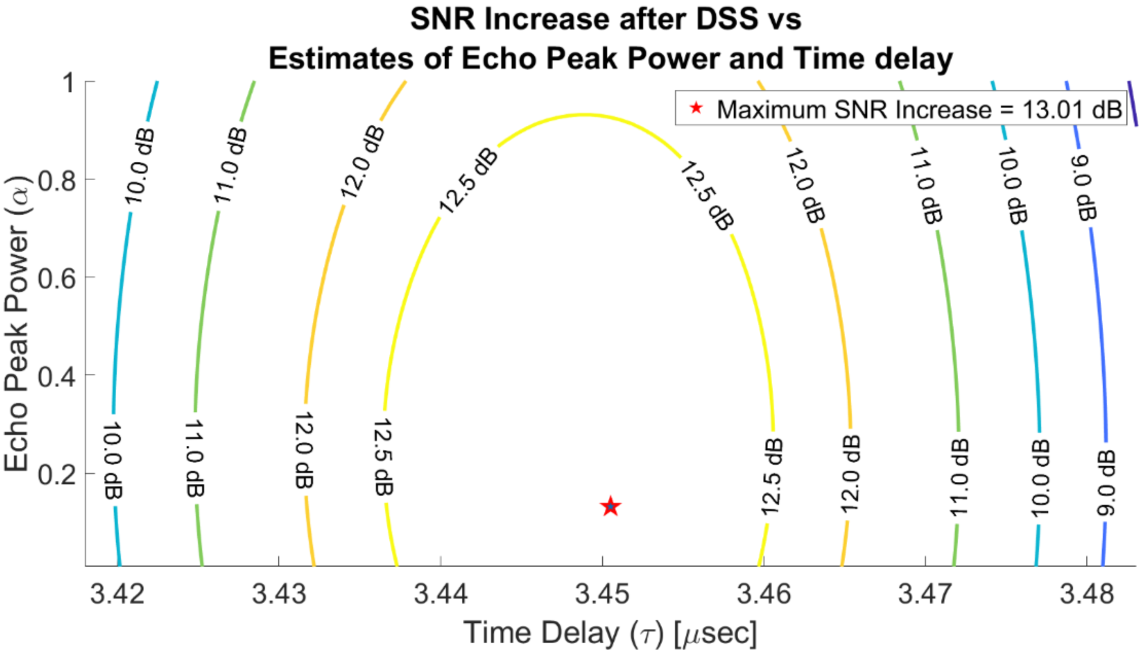

Results concerning deviating estimates of echo peak power and time delay used to construct the Wiener deconvolution filter are presented. The star indicates the case of optimum estimation of τ and α is achieved, which would provide the best possible SNR increase of 13.01 dB. Ellipses formed around the star indicate how the SNR will decrease with respect to suboptimal estimation of τ and α.

Figure 15. Increase in SNR after Applying the DSS Algorithm. Source: [2].

The key takeaway from Figure 15 is that a slight change in the estimated τ, on the order of a few μsec, will result in a loss of 3 dB or more in SNR, while the maximum loss due to poorly estimating α will only be at the order of 0.5 dB, which can be considered negligible compared to the losses due to τ. The crucial influence of the phase on SNR, which main component is the time delay, and the insignificance of the estimated amplitude of the impulse is potentially analogous to observations described in image recovery methods described by Shechtman et al. [39], research that highlights the importance of phase information for image recovery.

3. Optimum vs. Suboptimal Performance of DSS

The last part of the simulations regarding the ground-based single-channel passive radar case investigates the adverse effects of suboptimal estimation of τ. Applying DSS means updating the impulse response function for every new measurement. The continuous update of the impulse response function illustrates the adaptive character of DSS. To account for this, we iterated the algorithm for 10,000 simulations of white noise echo autocorrelation data for two cases: (1) optimum estimation of τ and (2) suboptimal estimation of τ within $\pm 0.5/f_s$ of optimum τ, which corresponds to ± 0.03 μsec change in τ. In Figure 16, the blue histograms correspond to performance of the radar without applying DSS, the orange histograms correspond to the radar results after performing DSS with suboptimal estimation of τ, and finally, the best case, depicted in the green histograms, when τ is optimally estimated.

The key takeaway of this figure is DSS's positive effect on the radar's performance, increasing its SNR substantially, which answers the question why it is essential to include DSS in systems with this architecture, which was highlighted by Peters et.al [14]. Furthermore, another important result highlighted by this figure is the significance of effective estimation of time delay when applying the filter, because suboptimal estimation will reduce the SNR of the radar.

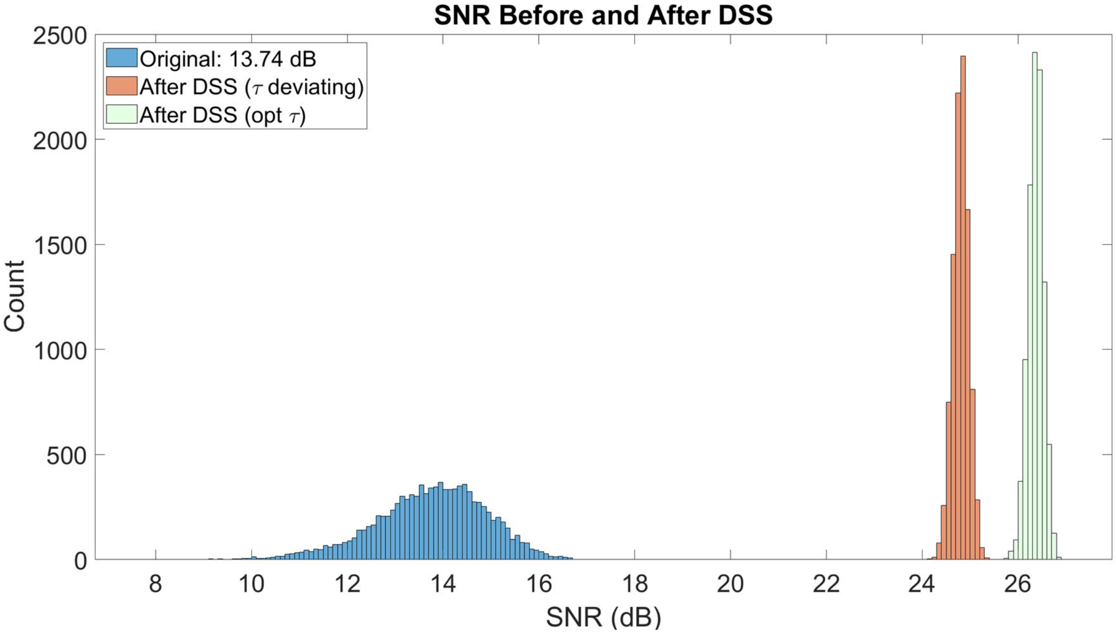

Comparison of the performance of a ground-based, stationary, single-channel passive radar before (blue histograms) and after applying DSS. Applying DSS was investigated for two cases, one with an optimum estimation of τ (green) and one where τ deviates (orange) around the optimum value ($\tau_0 \pm 0.5/f_s$).

Figure 16. SNR before and after DSS. Source: [2].

Figure 17 is a zoomed-in version of Figure 16 focused on the results for the two cases of τ, optimum estimation or deviation around the optimum value. Similar to the previous figure, we examine the extent to which the value of τ used in the Wiener filter diverges from the actual value, within a range of approximately ± 0.5/fs. Due to the adaptive character of DSS algorithm, the filter will run at every measurement. The mean loss in SNR, for all the different measurements, comes to 1.57 dB. This decrease in SNR only depicts a small error in the estimation of time delay used in the filter, that estimates the direct path. However, as described in chapter 2, there are many factors that if not accounted properly, can generate errors of the order of a few μsec, like this illustrated in this figure.

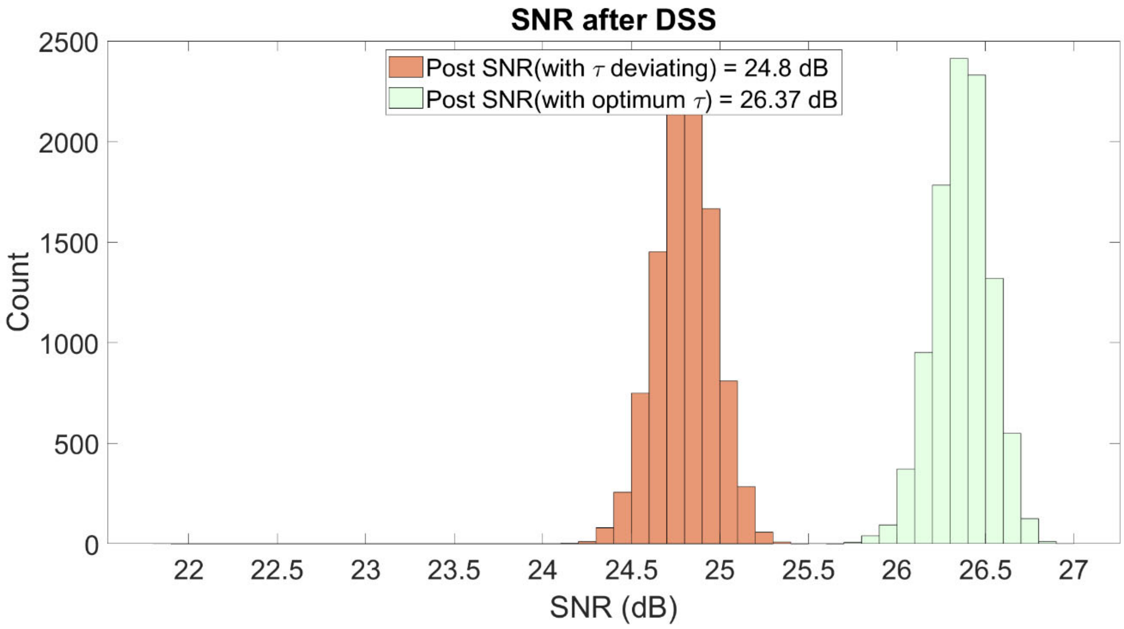

Results of applying DSS in SNR for two cases, one with an optimum estimation of τ (green), and one where τ deviates (orange) around optimum value ($\tau_0 \pm 0.5/f_s$).

Figure 17. SNR after DSS

Finally, Figure 18 presents the equivalent result of Figure 17 in terms of SNR increase, from not even applying DSS and applying DSS for the two cases described above. As above, the orange histograms correspond to the results after performing DSS with suboptimal estimation of τ, where an SNR increase of 11.06 dB was achieved, and the green histograms correspond to absolute estimation of time delay, resulting in a 12.62 dB increase in SNR. The important outcome highlighted by Figure 18 is that even though suboptimal estimation of time delay will not result in the best possible SNR, it will still generate a significant increase in SNR.

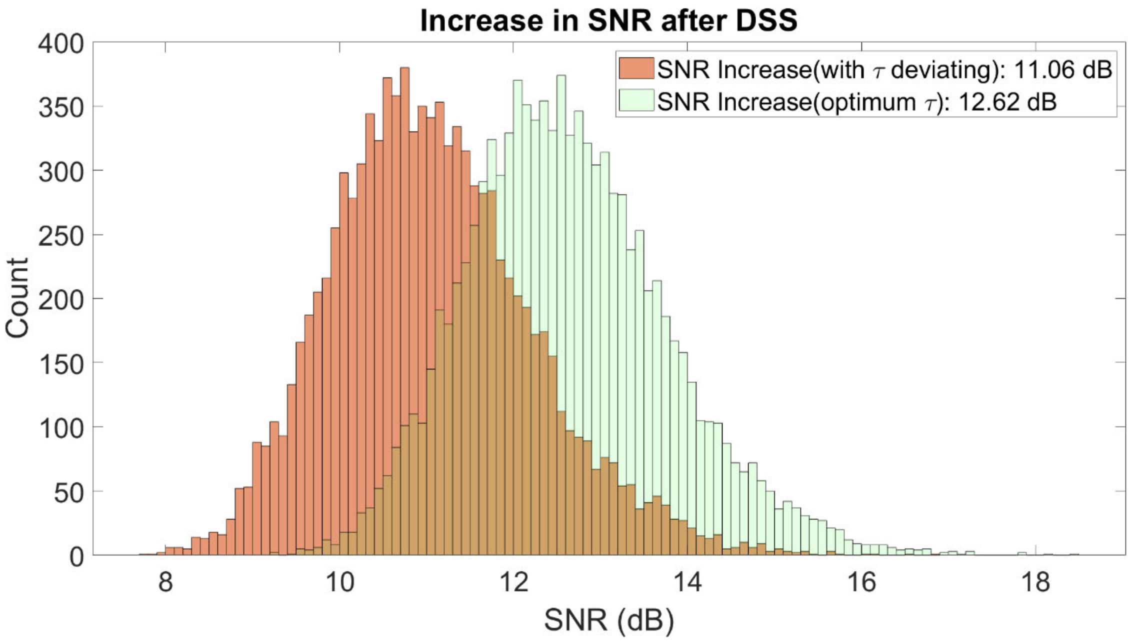

Results of applying DSS in overall increase of SNR for two cases, one with an optimum estimation of τ (green), and one where τ deviates (orange) around optimum value ($\tau_0 \pm 0.5/f_s$).

Figure 18. Increase in SNR after DSS. Source: [2].

IV. EFFECTS OF TEC ON SNR

A. INTRODUCTION

Total Electron Content (TEC) can be defined as the summation of the number of free electrons along a path between two points. In radar applications, those two points are usually the transmitter and the receiver, the two ends of the system. However, TEC has been broadly investigated due to its effects on a variety of applications, from satellite communications to High Frequency (HF) communications, and from traditional long-range radars to space-based radars and GPS signals (Global Positioning System).

Electrons populate every path between two points in a different content. This also applies to the case of a space asset, like the space-based radar we are investigating. However, in the propagation path through Earth's atmosphere, the region that is the main contributor to TEC is the ionosphere. By measuring TEC, scientists and engineers gain valuable insights into ionospheric conditions, allowing for more accurate predictions and corrections in various technological applications, such as communications, remote sensing, and GPS. TEC is measured in the number of electrons per square meter, usually reported in TEC units (TECU), which are 10^{16} electrons per m^2.

Figure 19 presents the electron density versus altitude for different layers of the atmosphere, from Earth's surface up to altitude over 1000km, verifying that the ionosphere is the main contributor to TEC. Also, the different layers of Earth's atmosphere defined with respect to temperature and ionization are presented. The ionization layers are labeled sequentially D, E, F1, and F2 from low to high altitude. Electron density is highest in the F2 region. Various satellite applications that can potentially be affected by TEC are illustrated on the right side of the figure.

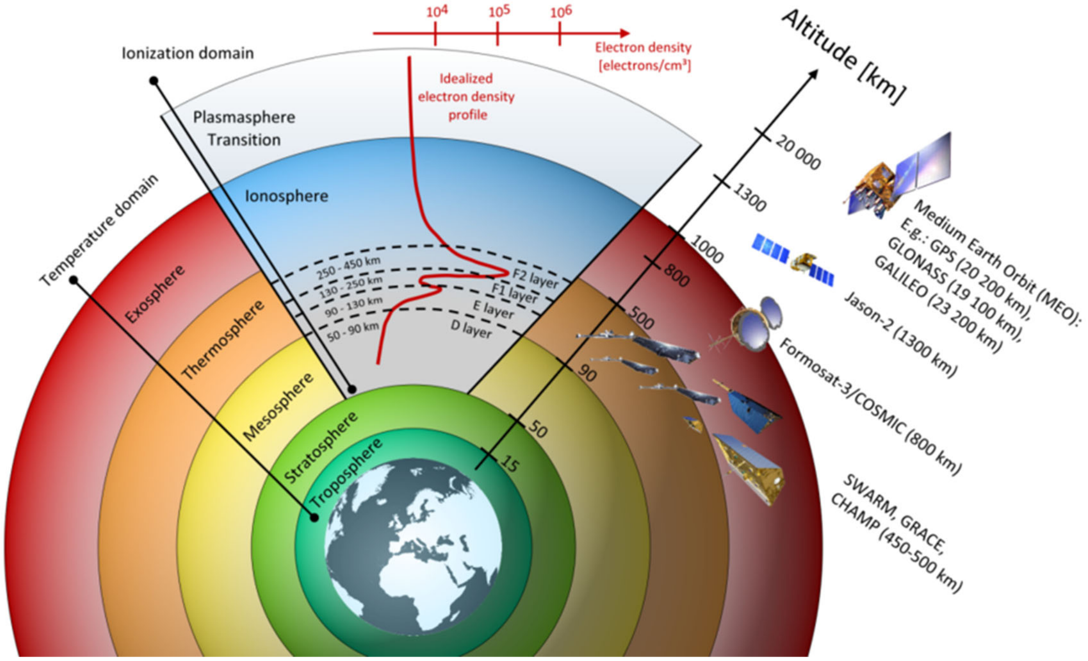

Electron density of various parts of the atmosphere, from Earth's surface up to altitude over 1000km. The ionosphere appears to contribute the most, where the peak TEC can be found. D, E, F1, and F2 refer to further ionosphere division, affecting the various applications differently. On the right side of the figure, various satellite applications that can potentially be affected by TEC are presented.

Figure 19. Electron Density vs. Altitude of an Idealized Ionospheric Profile. Source: [40].

Other parameters that affect TEC, apart from the specific layer of atmosphere, are illustrated as follows:

- Location: TEC values vary with geographical location, where they appear to be higher near the equator and then decreasing while going to the poles. However, this difference is not stationary for all longitudes and is affected by other factors [41], [42].
- Seasonal variations (e.g., equinoxes and solstices): Changes in solar angle and heating patterns in the Earth's atmosphere affect TEC, generating seasonal patterns [41], [42].

- Time of Day: TEC values typically vary throughout the day, with higher values observed during daytime and lower at night. This diurnal variation is due to solar radiation during the day, which enhances ionization in the ionosphere [41], [42].
- Solar activity: Solar radiation and solar flares significantly impact the ionization levels in the ionosphere [43].

B. TEC OVER GREENLAND

1. Methodology

In this research we are interested in extracting information regarding ice sheets in polar regions by using a space-based single-channel radar to measure the thickness and melt rates of ice sheets, therefore we will focus on TEC over Greenland and how these values affect the SNR of the radar. The knowledge a priori of TEC on the area where the satellite will operate is essential because TEC, as described in the previous chapter, leads to undesired phase shifts of the signal. This, if not accounted for correctly, can have negative effects on the radar's performance.

Due to the potential impacts of TEC on space applications, various techniques have been developed to accurately estimate TEC; one of the most common is measuring the phase shift generated due to the difference between frequencies of GNSS signals [44]. To better estimate and predict TEC accurately, software models have been developed allowing one to estimate TEC based for various input conditions.

In this chapter, we will focus on calculating the phase shift due to TEC for the region of Greenland with respect to selected variables and then calculate the corresponding time delay. Recalling information from the previous chapter of this thesis, the phase shift for a 2-way propagation path is given by equation (10). It is important to note that in our case, the actual phase difference will slightly deviate from what is presented here due to the geometry of the problem and the different propagation path that solar emission follows from the Sun to Earth's surface and then after being reflected to the base of the ice sheet, back to the receiver of the radar. Due to the different scenarios that can exist, based on the locations of the Sun and the radar with respect to Earth's surface, we know that the actual phase difference will deviate slightly from the estimate given by the equation (10). However, extracting the exact phase difference formula for all the possible geometries is not the subject of this research; we will instead focus on the impact of the radar's SNR, using equation (10) as given. Then, from the equation, one can translate the phase difference $\Delta\Phi_{2\text{-way}}$ to signal time delay by using [30], [31]

$$\Delta t = \frac{\Delta\Phi_{2-way}}{2\pi f} \tag{19}$$

where f is the frequency of the signal in Hz.

Conceptually continuing from Chapter III, and especially from Figure 12, where the signal processing flow of the algorithm was presented, the time delay of the received signal should be accounted for and subtracted while building the deconvolution filter to optimize the radar results.

Furthermore, another crucial thing to note is that from equation (10), one can calculate the phase difference for a 2-way propagation based on TEC along a vertical path, also known as VTEC. However, this means that the propagation path will strictly be at the nadir of the satellite, which is not the case in our problem. Instead of VTEC, the more appropriate values for this problem is the Slant TEC or STEC (Slant Total Electron Content). Figure 20 helps to visualize the difference between VTEC and STEC. In the figure, the vertical, dark blue line perpendicular to Earth's surface represents VTEC, while the actual signal follows a different path indicated by the red line, associated with a STEC, which is larger than the VTEC given the longer path length. The penetration angle in the ionosphere, indicated by 'z' in the figure, controls the difference between VTEC and STEC, and as 'z' increases so does STEC relative to VTEC. However, as before, due to the large number of possible geometries and the different paths the incoming signal will travel, calculating the STEC is beyond the scope of this research and is left as potential future work. We will instead use the VTEC as a representative proxy.

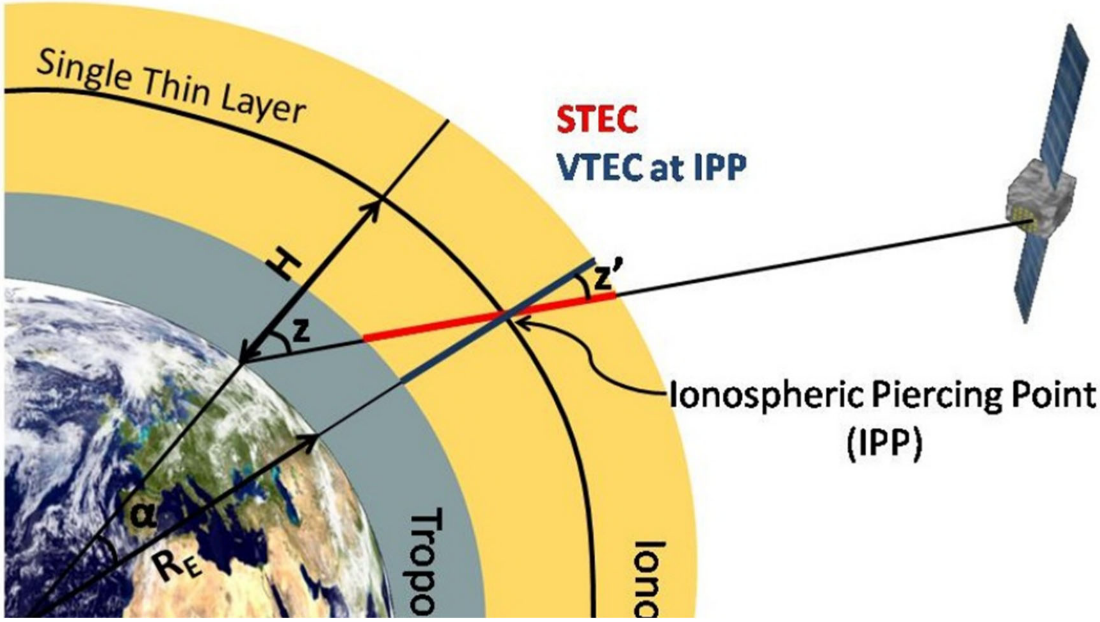

The dark blue line illustrates the vertical path the signal would follow in the case of a nadir-facing space-based radar, where VTEC would be the appropriate value to calculate $\Delta\Phi_{2\text{-way}}$. In the case of non-nadir facing radars, the emission will follow a slant path corresponding to STEC. The angle z is the angle of penetration of the ionosphere, which controls the difference between VTEC and STEC.

Figure 20. Vertical and Slant TEC. Source: [45].

2. TEC Data

In this research, we used VTEC data calculated using the International Reference Ionosphere (IRI) model, which is available online [46]. Table 4 presents an overview of the IRI model's data inputs and other helpful information on the simulation setup. While presenting each figure, more information based on the exact simulation setup will be provided.

Table 4. Data Setup – IRI Model

Data setup – IRI model	
IRI version	**2016**
Time	Varying based on the plot
Year	2022 1961-2022
Coordinates	**Central Greenland**
	Lat: 75°N **Lon**: 40°W
Coordinates	**Greenland**
	Lat: 65°N-85°N **Lon**: 60°W-20°W
Height	**500km**
Profile Type	Varying based on the plot

3. TEC Results

Figure 21 presents the VTEC calculated at Lat: 75°North – Lon: 40°West, which is a central position of Greenland, for every day during calendar year 2022 at 17:00 LT (Local Time). In this figure, one can see the variation of VTEC over a whole year, which must be accounted for when making radar measurements at this location. These values correspond to specific time of day, but actually TEC varies continuously as a function of hour, day, and year. The time (1700 LT) was chosen as it typically represented the highest VTEC values on most days. This means the equivalent plot corresponding to a different hour of the day would look similar with reduced values.

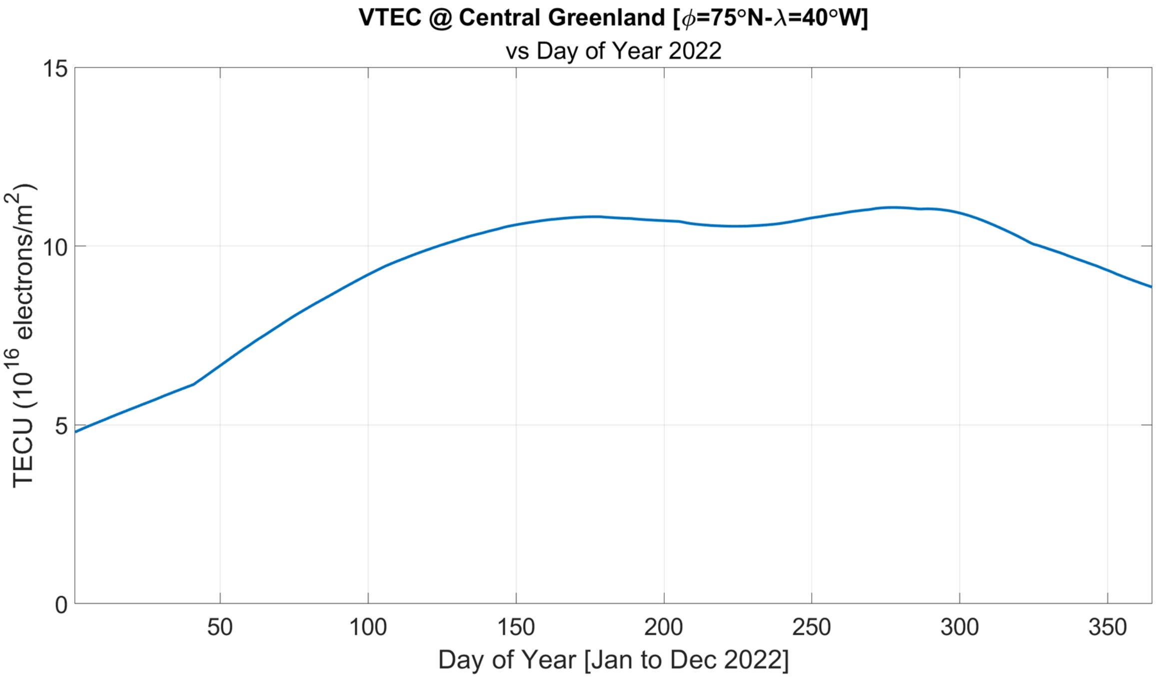

VTEC at a central location of Greenland (Lat:75°N-Lon:40°W) during 2022, at 17:00 LT, with intervals of one day. We start from January at the left side of the figure and proceed throughout the year to December at the right side.

Figure 21. VTEC at Central Greenland in 2022.

Another parameter that affects TEC is the solar cycle. The Sun experiences a recurring pattern known as the solar cycle, lasting approximately 11 years. During this cycle, the Sun's magnetic field undergoes a complete reversal, meaning the positions of its north and south poles switch. It then takes another 11 years for the magnetic poles to revert to their original positions. This solar cycle significantly influences surface activity on the Sun, leading to phenomena like sunspots, which result from changes in the Sun's magnetic fields [46]. One of these phenomena is the variation of TEC of the ionosphere during these periods. Figure 22 presents the VTEC at a central location of Greenland (Lat:75°N-Lon:40°W) at 17:00 LT on January 1st of each year from 1961 to 2022, with one-year intervals. From this figure, one can see the effects of the solar cycle on the TEC of Earth's ionosphere, which should be accounted for, as it will change the time delay of the received signal. As before, 17:00LT was chosen because it typically represents the maximum value of VTEC on a given day. Another important thing to notice from Figure 22 are the red and yellow stars, which indicate the two extreme values of VTEC, which varies from the maximum value of 19.4 TECU to a minimum of 1.3 TECU over the entire plot.

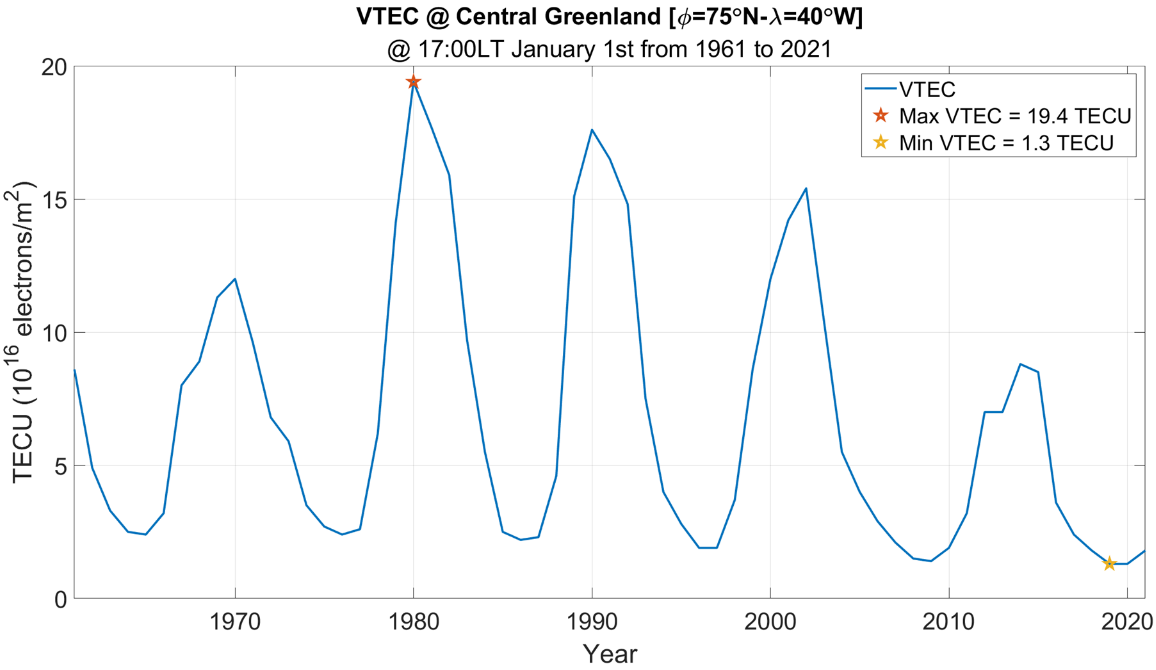

VTEC at a central location of Greenland (Lat:75°N-Lon:40°W) at 17:00 LT on January 1st of each year from 1961 to 2022, with one-year intervals.

Figure 22. VTEC at Central Greenland from 1961 to 2022.

Figure 23 illustrates the same concept as the previous two graphs, where VTEC was presented for a central location in Greenland. In this figure, VTEC is given with respect to hours of four specific days of FY 2022, spring and fall equinoxes, and summer and winter solstices. This figure shows the similarities between the four plots, as they follow the same pattern, with maximum values appearing in the afternoon and minimum values during night hours. A key takeaway of this figure is that over the course of a given day, the VTEC typically ranges from a value of 11.7 to 3.3 TECU, values represented with the green and blue stars respectively.

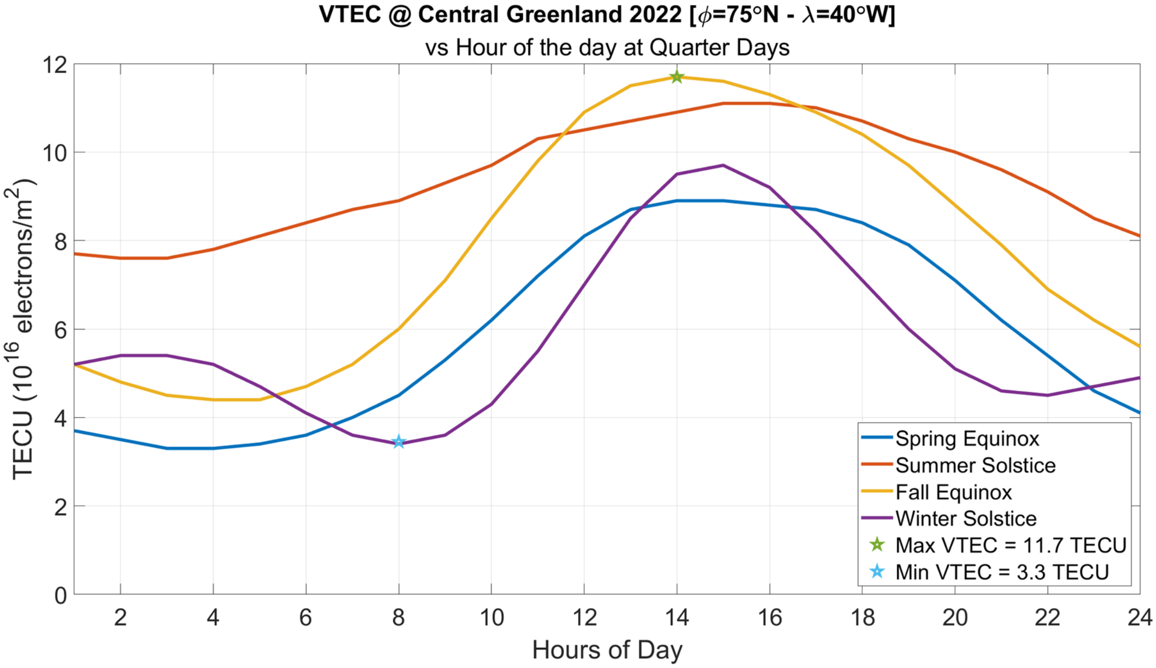

VTEC at a central location of Greenland (Lat:75°N-Lon:40°W) during the quarter days (spring and fall equinoxes and summer and winter solstices) of FY 2022.

Figure 23. VTEC at Central Greenland at Quarter Days of 2022.

Figure 24 presents a contour plot of the VTEC calculated over a range of locations in Greenland, from 60–85 degrees North and 290–340 degrees East. All values were calculated at 15:00 UTC (Universal Coordinated Time), on January 1st, 2022. At the x and y axes, the longitude and the latitude of its particular location are depicted respectively. On the right side of the figure, a color bar indicates the colors corresponding to each TECU value. This figure presents only one glimpse of VTEC for the whole area of Greenland. To be consistent, the exact figure should be generated for each specific hour of each day for this area over the time the satellite will orbit Greenland and take the respective measurements. In this case, after considering the actual propagation path of radiation, we could calculate the equivalent phase difference and then the time delay. Subtracting this from the received signal would be crucial for the performance of the radar.

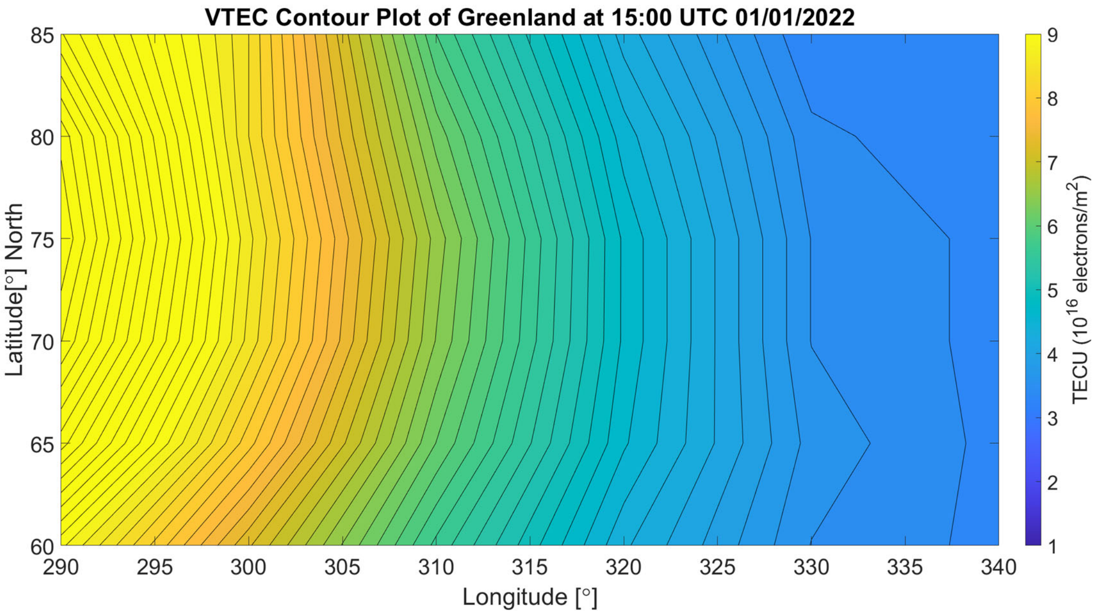

VTEC calculation for the whole region that Greenland covers. At the x and y axes, the longitude and the latitude of its specific location are depicted respectively, values that correspond to Greenland's position on the globe. The color bar at the right side of the figure corresponds to the values of TEC.

Figure 24. VTEC Contour Plot of Greenland at 15:00 UTC on 01/01/2022.

C. TIME DELAY DUE TO TEC FOR GREENLAND

As described in the first section of the current chapter, VTEC corresponds to a phase difference of the electromagnetic signal calculated using equation (10). Then, using the phase difference, we can calculate the corresponding time delay from equation (19),. Figure 25 is equivalent of Figure 23, but now showing the variation time delay over four days in 2022. The time delay due to the ionosphere is not negligible. Of course, other phase errors, such as those described in Chapter II, will generate respective time delays that must also be considered.

Figure 25 presents the time delay in μsec for four specific days of FY 2022, the spring and fall equinoxes, and summer and winter solstices. In this figure, as in Figure 23, one can see the apparent similarities between the four plots, as they follow the same pattern, with the maximum time delay occurring in the afternoon and minimum values during night hours. Note, the time delay shown in Figure 25 has been calculated for a frequency of 330MHz, which is the planned frequency of the radar for this experiment, as presented in

0. The time delay would differ for a radar with different operating frequencies. Also, by putting together equations (10) and (19), one can see that the time delay is inversely proportional to the square of the operating frequency. In other words, time delay decreases with increasing frequencies.

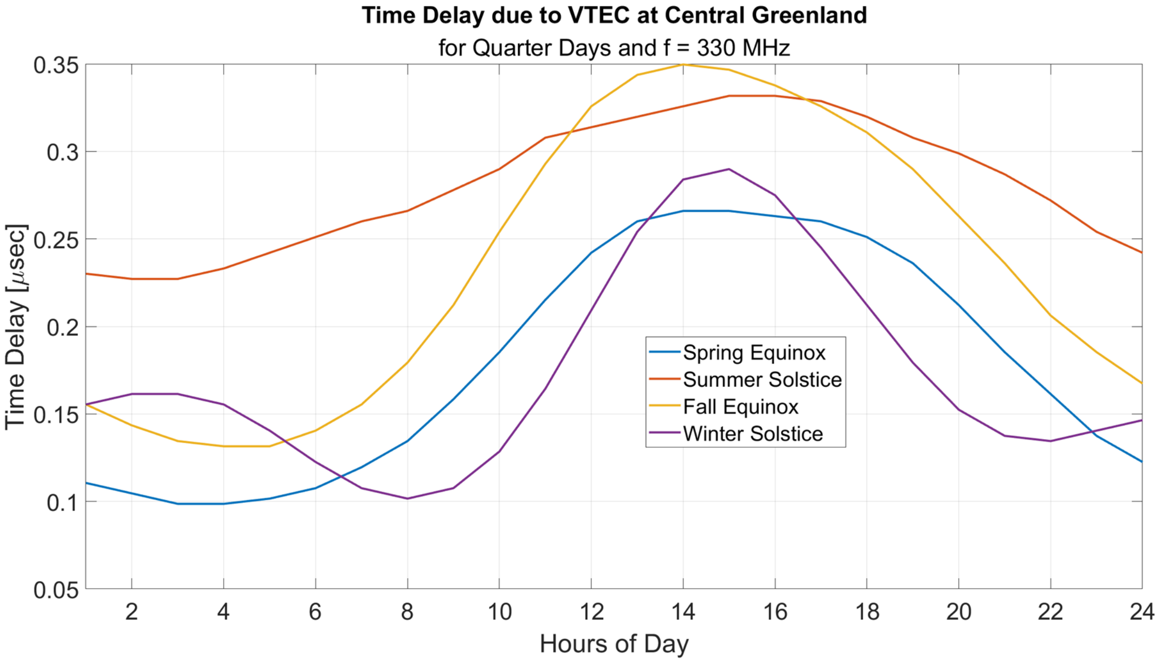

Time Delay at a central location of Greenland (Lat:75°N-Lon:40°W) during the quarter days (spring and fall equinoxes and summer and winter solstices) of FY 2022 for an operating frequency of 330MHz, which is the frequency of the passive radar presented in Chapter III.

Figure 25. Time Delay at Central Greenland at Quarter Days of 2022 for f=330MHz.

Based on the above figures, the VTEC over Greenland can be expected to vary between a maximum of roughly 19.4 TECU and a minimum of 1.3 TECU. From this we can calculate the maximum time delay due to VTEC for all the operating frequencies of interested. Figure 26 presents the VTEC time delay for a frequency range extending from MHz to GHz. This figure is also generated with values of VTEC for central Greenland, calculating the maximum and minimum values from 1961 to 2022. The time delays of the investigated frequency range that corresponds to the maximum value of 19.4 TECU and the minimum of 1.3 TECU are represented by the blue and red lines respectively. Four important frequencies are noted with stars in this plot. It starts with 9MHz, a vital frequency for terrestrial analog passive-sounding development, the same frequency as the instrument used in RIME/REASON missions. The next frequency illustrated is 30 MHz, which is the most likely frequency to be used in the passive Jovian burst demo because it is above the ionospheric cutoff frequency and Jupiter bursts exist in this band. Next, 300 MHz is the frequency currently used for passive sounding in Greenland, also indicated by the green box. Finally, 1GHz is shown because it has potential for future passive testing for altimetry purposes. Figure 26 provides insight into this frequency band's maximum and minimum time delay errors, that range from 0.0522 to the minimum value of 3.2613×10^{-9} seconds.

D. EFFECT OF TEC ON SNR

One common issue encountered in space communication and space-based radars is the existence of phase errors due to electromagnetic waves traveling through the ionosphere and interacting with free electrons. As described in this thesis, with a priori knowledge of VTEC we can estimate those phase errors and the equivalent time delay.

In chapter 3, we explored the effect inaccurate values of τ, meaning time delay, has on the SNR and the overall performance of the radar. However, we did not account for phase errors due to VTEC. As identified in this chapter and shown in Figure 26, the potential time delay is not negligible and must be included. From Figure 26, we can obtain the minimum and maximum values of time delay for the operating frequency of our radar (330MHz), which are 3.89×10^{-8} and 5.798×10^{-7} seconds, respectively.

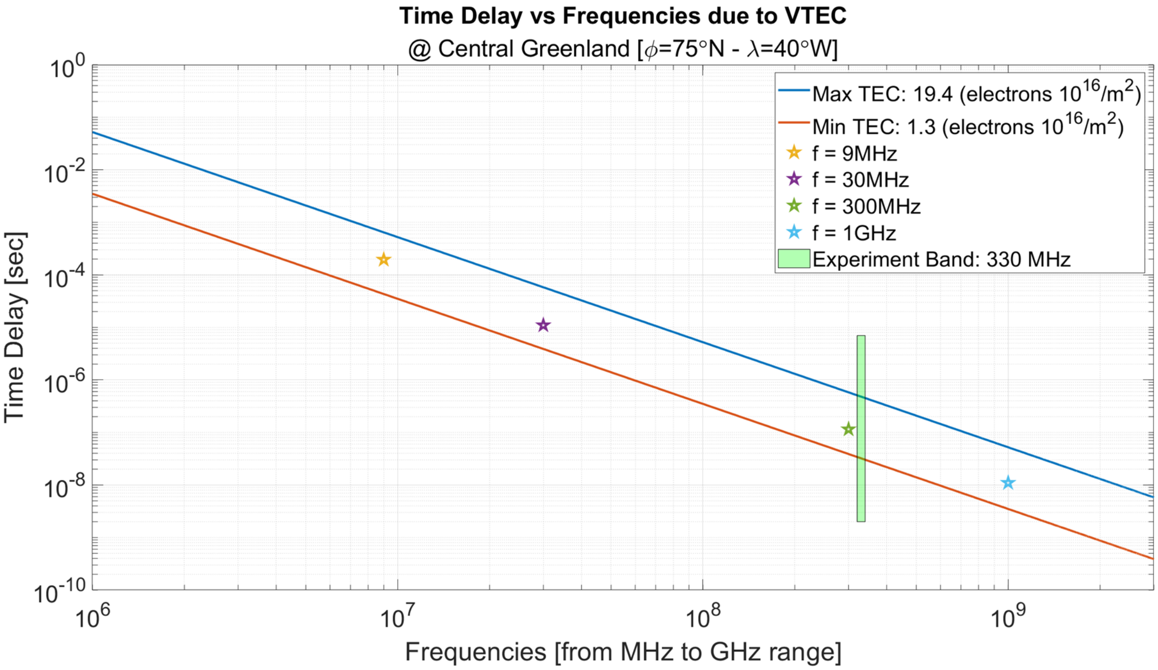

Maximum and minimum time delay at a central location of Greenland (Lat:75°N-Lon:40°W) for a frequency range from MHz to GHz. The corresponding maximum and minimum values of VTEC used to generate this plot are shown in the legend. The blue line corresponds to the time delays within the investigated frequency range, where the VTEC reaches its maximum value of 19.4 TECU, while the red line represents the time delays for the minimum value of 1.3 TECU. Time delays of four individual frequencies are indicated with stars due to the importance of those to passive radar-sounding experiments. The band of the experiment held in this research is also highlighted with green color.

Figure 26. Time Delay due to VTEC for a Frequency Range from MHz to GHz.

Figure 27 presents the results of 10,000 autocorrelations of synthetic data. The simulations generated a VTEC time delay that varies by $\pm\ 5.798 \times 10^{-7}$ seconds, the worst-case scenario for our frequency band. In this figure, which is the equivalent of Figure 13 from Chapter III, one can see the SNR's strong dependence on the deconvolution filter's estimated time delay, and how not accounting for TEC can diminish the performance of the passive radar. The x-axis represents the value of the estimated time delay, which we insert into the deconvolution filter, aiming to accurately estimate the direct path signal. As we can see in Figure 27, in the case of optimal time delay estimation, we will get the maximum possible SNR, represented by the main lobe. However, as the value of our estimation for time delay recedes from the correct value of 3.45μsec, SNR reduces significantly. Apart from the main lobe, some nulls and sidelobes create a decaying 'sinc' function pattern, the SNR decreases. The red dashed line indicates the -3dB margin, a reasonable figure of merit as it illustrates the case where the received signal has half the power of the original. However, in the case we investigate, the power of the received signal does not change. As this research shows, inaccurate estimates of time delay will generate the lower SNR depicted at Figure 27, which in this case are due to VTEC. In contrast, the blue dashed line shows the time delay the signal would have if it did not propagate through the ionosphere.

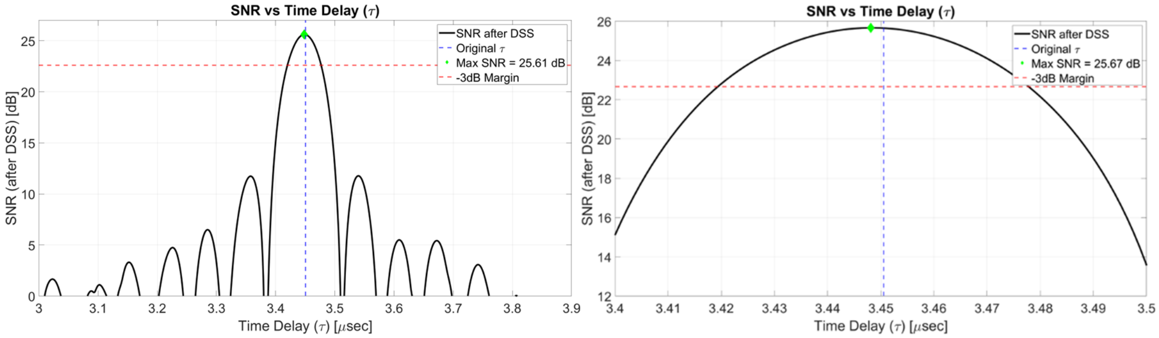

(Left) SNR vs. a varying estimated time delay (τ) due to signal propagating through the ionosphere and interacting with free electrons. The time delay value corresponds to the estimated value being input at the Wiener deconvolution filter, used to estimate the direct path. Results are based on 10,000 autocorrelations of synthetic data. The red dashed line illustrates the -3dB margin, a common figure of merit indicating reception of half power. In contrast, the blue dashed line illustrates the actual time delay, one that the signal would have if it did not propagate through the ionosphere. Adapted from [2]. (Right) Zoomed in version of the left panel.

Figure 27. Dependence of SNR on Delay Time (τ) – Revision of Figure 13. Adapted from [2].

V. CONCLUSION

A. SUMMARY OF RESULTS

This thesis focused on optimizing the performance of a single-channel passive radar, which uses ambient noise solar emissions. Passive radars offer unique advantages that complement the Navy’s radar capabilities and operational strategies. One of the many advantages of this type of sensor is that it can operate in challenging environments such as polar regions or outer space and contribute to the success of a wide range of naval-air-space missions. A passive radar uses an existing DSS signal processing algorithm, which was the target of optimization of this research. The center of investigation regarding DSS was the time delay, τ, and echo peak power, α; the two parameters input into the Wiener deconvolution filter, in order to estimate the signal received directly from the Sun.

The first part of the thesis presented the impact of suboptimal estimation of τ and α on the performance of the radar. Our results emphasize the significant role that τ has on the SNR of the radar and that even small divergence from its original value significantly reduce the SNR. On the other hand, our findings also highlight that even substantial changes in α will lead to only a slight reduction in SNR. Moreover, the adaptive nature of the algorithm is highlighted since the purpose of the deconvolution filter is to continually refine the approximation of the direct signal’s waveform, resulting in the need for continuous estimates of the time delay, τ.

The second part focused on how TEC and propagation through this region of the atmosphere can affect the SNR of the radar. TEC values were estimated using the International Reference Ionosphere model and used to calculate the corresponding time delay due to propagation through the ionosphere for a variety of scenarios involving space-based single-channel passive radar measurements of Greenland. The TEC time delays for critical passive sounding frequencies were also calculated. Our results indicate that the time delay due to TEC is comparable to the actual time delay and therefore not negligible. Finally, a revision of results from the previous section, Chapter III, was made by finding the SNR dependence on TEC time delay due to TEC; the results indicate the severe impact that TEC can have on the SNR of the radar if not accounted for properly.

B. FUTURE WORK

Passive radar sounding offers a low-resource remote sensing technique that can be implemented with zero architecture modifications and provides continuous measurements of ice sheets' thickness and melt rates. However, many steps are still required to make low-resource space-based remote sensing feasible. Recommended next steps include:

- Calculate the phase errors and the corresponding time delay due to clutter caused by surface reflections with varying roughness.
- Investigate the potential consequences for the Doppler phase shift.
- Estimate the slant TEC (STEC) for relevant geometries based off the VTEC (e.g., Sun's emissions – Earth's surface – receiver).
- Calculate the exact phase difference formula for all the possible geometries of the problem and then integrate this with the estimated STEC.
- Develop a model to provide continuous values of STEC for the whole region of interest (Greenland), considering all the phenomena that affect TEC.

LIST OF REFERENCES

[1] H. D. Griffiths and C. J. Baker, "An introduction to passive radar," *The Aeronautical Journal*, vol. 121, no. 1244, pp. 1601–1603, 2017. doi: 10.1017/aer.2017.85.

[2] A. Lamprou and S. T. Peters, "Optimization of adaptive direct signal suppression for single-channel passive radar sensing," in *IGARSS 2023 – 2023 IEEE International Geoscience and Remote Sensing Symposium*, Jul. 2023, pp. 4230–4233. doi: 10.1109/IGARSS52108.2023.10282895.

[3] "HENSOLDT's passive radar demonstrates its suitability for air traffic control." Accessed: Sep. 28, 2023. Available: https://www.hensoldt.net/news/hensoldts-passive-radar-demonstrates-its-suitability-for-air-traffic-control/

[4] R. Zemmari, M. Brötje, M. Feldmann, and U. Nickel, "Maritime surveillance with GSM passive radar: Detection and tracking of small agile targets," *Int. Radar Symp.*, vol. 1, pp. 245–251, Jan. 2013.

[5] S. T. Peters, D. M. Schroeder, M. S. Haynes, D. Castelletti, and A. Romero-Wolf, "Passive synthetic aperture radar imaging using radio-astronomical sources," *IEEE Transactions on Geoscience and Remote Sensing*, vol. 59, no. 11, pp. 9144–9159, Aug. 2021, doi: 10.1109/TGRS.2021.3050429.

[6] I. Theodorou, C. Ilioudis, C. Clemente, M. Vasile, and J. Soraghan, "SISAR imaging for space debris based on nanosatellites," *IET Radar, Sonar & Navigation*, vol. 14, no. 8, pp. 1192–1201, Aug. 2020, doi: 10.1049/iet-rsn.2019.0574.

[7] A. R. Persico, P. Kirkland, C. Clemente, J. J. Soraghan, and M. Vasile, "CubeSat-based passive bistatic radar for space situational awareness: A feasibility study," *IEEE Trans. Aerosp. Electron. Syst.*, vol. 55, no. 1, pp. 476–485, Feb. 2019, doi: 10.1109/TAES.2018.2848340.

[8] S. T. Peters *et al.*, "Glaciological monitoring using the sun as a radio source for echo detection," *Geophysical Research Letters*, vol. 48, no. 14, Jul. 2021, doi: 10.1029/2021GL092450.

[9] S. T. Peters, D. M. Schroeder, D. Castelletti, M. S. Haynes, and A. Romero-Wolf, “Two dimensional image formation with passive radar using the sun for echo detection,” in *IGARSS 2019 – 2019 IEEE International Geoscience and Remote Sensing Symposium*, Yokohama, Japan: IEEE, Jul. 2019, pp. 10091–10094. doi: 10.1109/IGARSS.2019.8897880.

[10] T. M. Roberts, A. Romero-Wolf, L. Bruzzone, L. Carrer, S. Peters, and D. M. Schroeder, “Conditioning Jovian burst signals for passive sounding applications,” *IEEE Transactions on Geoscience and Remote Sensing*, vol. 60, pp. 1–14, 2022, doi: 10.1109/TGRS.2021.3109106.

[11] H. Griffiths, “Klein Heidelberg: New information and insight,” in *2015 IEEE Radar Conference*, Johannesburg, South Africa: IEEE, Oct. 2015, pp. 527–532. doi: 10.1109/RadarConf.2015.7411939.

[12] W. Paper, L. Humbert, and T. Fountain, “An introduction to passive radar systems.” White paper. Munich, Germany: Rohde & Schwarz, 2023.

[13] A. Lamprou and S. T. Peters, “Optimization of adaptive direct signal suppression for single-channel passive radar sensing,” in *2023 IEEE International Geoscience and Remote Sensing Symposium IGARSS*, Jul. 2023.

[14] S. T. Peters, D. M. Schroeder, and A. Romero-Wolf, “Adaptive single-channel direct signal suppression for ambient noise passive radar sounding,” in *2021 IEEE International Geoscience and Remote Sensing Symposium IGARSS*, Jul. 2021, pp. 7912–7915. doi: 10.1109/IGARSS47720.2021.9554427.

[15] F. Wang, H. Li, X. Zhang, and B. Himed, “Signal parameter estimation for passive bistatic radar with waveform correlation exploitation,” *IEEE Trans. Aerosp. Electron. Syst.*, vol. 54, no. 3, pp. 1135–1150, Jun. 2018, doi: 10.1109/TAES.2017.2775898.

[16] S. T. Peters, D. M. Schroeder, D. Castelletti, M. Haynes, and A. Romero-Wolf, “In situ demonstration of a passive radio sounding approach using the sun for echo detection,” *IEEE Trans. Geosci. Remote Sensing*, vol. 56, no. 12, pp. 7338–7349, Dec. 2018, doi: 10.1109/TGRS.2018.2850662.

[17] A. Romero-Wolf, S. Vance, F. Maiwald, E. Heggy, P. Ries, and K. Liewer, “A passive probe for subsurface oceans and liquid water in Jupiter’s icy moons,” *Icarus*, vol. 248, pp. 463–477, Mar. 2015, doi: 10.1016/j.icarus.2014.10.043.

[18] D. M. Schroeder *et al.*, “Assessing the potential for passive radio sounding of Europa and Ganymede with RIME and REASON,” *Planetary and Space Science*, vol. 134, pp. 52–60, Dec. 2016, doi: 10.1016/j.pss.2016.10.007.

[19] S. T. Peters, “Passive radar sounding for terrestrial and planetary glaciology,” Ph.D., Stanford University, United States -- California, 2020. Accessed: Oct. 23, 2023. Available: https://www.proquest.com/docview/2593595621/abstract/D1B8BA0CC33D456DPQ/1

[20] “Analytic approximations of scattering effects on beam chromaticity in 21-cm global experiments.” Accessed: Oct. 08, 2023. Available: https://www.researchgate.net/publication/365887906_Analytic_approximations_of_scattering_effects_on_beam_chromaticity_in_21-cm_global_experiments

[21] W. M. Goss, C. Hooker, and R. D. Ekers, “Sea-cliff interferometry: Dover heights, 1946,” in *Joe Pawsey and the Founding of Australian Radio Astronomy: Early Discoveries, from the Sun to the Cosmos*, W. M. Goss, C. Hooker, and R. D. Ekers, Eds., in Historical & Cultural Astronomy. , Cham: Springer International Publishing, 2023, pp. 357–375. doi: 10.1007/978-3-031-07916-0_13.

[22] K. Kulpa, “The CLEAN type algorithms for radar signal processing,” in *2008 Microwaves, Radar and Remote Sensing Symposium*, Sep. 2008, pp. 152–157. doi: 10.1109/MRRS.2008.4669567.

[23] C. Gerekos, L. Bruzzone, and M. Imai, “A coherent method for simulating active and passive radar sounding of the Jovian icy moons,” *IEEE Trans. Geosci. Remote Sensing*, vol. 58, no. 4, pp. 2250–2265, Apr. 2020, doi: 10.1109/TGRS.2019.2945079.

[24] “A coherent multilayer simulator of radargrams acquired by radar sounder instruments | RIME.” Accessed: Oct. 08, 2023. Available: https://rslab.disi.unitn.it/rime/a-coherent-multilayer-simulator-of-radargrams-acquired-by-radar-sounder-instruments/

[25] G. P. Blasone, F. Colone, P. Lombardo, P. Wojaczek, and D. Cristallini, “A two-stage approach for direct signal and clutter cancellation in passive radar on moving platforms,” in *2019 IEEE Radar Conference (RadarConf)*, Boston, MA, USA: IEEE, Apr. 2019, pp. 1–6. doi: 10.1109/RADAR.2019.8835704.

[26] D. Bekaert *et al.*, “Multichannel surface clutter suppression: East Antarctica P-band SAR ice sounding in the presence of grating lobes,” *Ann. Glaciol.*, vol. 55, no. 67, pp. 9–21, 2014, doi: 10.3189/2014AoG67A100.

[27] R. Culberg and D. M. Schroeder, “Firn clutter constraints on the design and performance of orbital radar ice sounders,” *IEEE Trans. Geosci. Remote Sensing*, vol. 58, no. 9, pp. 6344–6361, Sep. 2020, doi: 10.1109/TGRS.2020.2976666.

[28] B. Shraddha, *Mobile Radio Propagation: Small Scale Fading*. New York, USA: Prestige Institute, 2015.

[29] J. Hospodka, “Doppler shift satellite navigation – NAVSAT-TRANSIT and adherents,” *MAD*, vol. 1, no. 2, p. 11, Mar. 2013, doi: 10.14311/MAD.2013.02.03.

[30] C. Grima, D. D. Blankenship, and D. M. Schroeder, “Radar signal propagation through the ionosphere of Europa,” *Planetary and Space Science*, vol. 117, pp. 421–428, Nov. 2015, doi: 10.1016/j.pss.2015.08.017.

[31] S. T. Peters, D. M. Schroeder, and A. Romero-Wolf, “Passive radio sounding to correct for Europa’s ionospheric distortion of VHF signals,” *Planetary and Space Science*, vol. 187, p. 104925, Aug. 2020, doi: 10.1016/j.pss.2020.104925.

[32] J. L. Garry, C. J. Baker, and G. E. Smith, “Evaluation of direct signal suppression for passive radar,” *IEEE Trans. Geosci. Remote Sensing*, vol. 55, no. 7, pp. 3786–3799, Jul. 2017, doi: 10.1109/TGRS.2017.2680321.

[33] J. L. Garry, G. E. Smith, and C. J. Baker, “Direct signal suppression schemes for passive radar,” in *2015 Signal Processing Symposium (SPSympo)*, Debe, Poland: IEEE, Jun. 2015, pp. 1–5. doi: 10.1109/SPS.2015.7168278.

[34] M. H. Hayes, *Statistical Digital Signal Processing and Modeling.* New York, USA: John Wiley & Sons, 1996.

[35] A. U. Al-Saggaf, M. Arif, U. M. Al-Saggaf, and M. Moinuddin, “The q-normalized least mean square algorithm,” in *2016 6th International Conference on Intelligent and Advanced Systems (ICIAS)*, Kuala Lumpur, Malaysia: IEEE, Aug. 2016, pp. 1–6. doi: 10.1109/ICIAS.2016.7824098.

[36] R. G. Brown and P. Y. C. Hwang, *Introduction to random signals and applied Kalman filtering: with MATLAB exercises and solutions*, 3rd ed. New York, USA: Wiley, 1997.

[37] F. Colone, C. Palmarini, T. Martelli, and E. Tilli, “Sliding extensive cancellation algorithm for disturbance removal in passive radar,” *IEEE Trans. Aerosp. Electron. Syst.*, vol. 52, no. 3, pp. 1309–1326, Jun. 2016, doi: 10.1109/TAES.2016.150477.

[38] T. J. Cornwell, “Hogbom’s CLEAN algorithm. Impact on astronomy and beyond: Commentary on: Högbom J. A., 1974, A&AS, 15, 417,” *A&A*, vol. 500, no. 1, pp. 65–66, Jun. 2009, doi: 10.1051/0004-6361/200912148.

[39] Y. Shechtman, Y. C. Eldar, O. Cohen, H. N. Chapman, J. Miao, and M. Segev, “Phase Retrieval with Application to Optical Imaging: A contemporary overview,” *IEEE Signal Process. Mag.*, vol. 32, no. 3, pp. 87–109, May 2015, doi: 10.1109/MSP.2014.2352673.

[40] “DGFI-TUM – Atmosphere.” Accessed: Oct. 24, 2023. Available: https://www.dgfi.tum.de/en/research/cross-cutting-research-topics/atmosphere/

[41] “Analysis of total electron content (TEC) variations in the low- and middle-latitude ionosphere – ProQuest.” Accessed: Oct. 24, 2023. Available: https://www.proquest.com/openview/bcafa7634f551e27475994dd4537e979/1?pq-origsite=gscholar&cbl=18750

[42] C. Cai, “Monitoring seasonal variations of ionospheric TEC using GPS measurements,” *Geo-spat. Inf. Sc.*, vol. 10, no. 2, pp. 96–99, Jun. 2007, doi: 10.1007/s11806-007-0034-z.

[43] D. R. Themens and P. T. Jayachandran, “Solar activity variability in the IRI at high latitudes: Comparisons with GPS total electron content,” *Journal of Geophysical Research: Space Physics*, vol. 121, no. 4, pp. 3793–3807, 2016, doi: 10.1002/2016JA022664.

[44] G. K. Seemala, “Chapter 4 – Estimation of ionospheric total electron content (TEC) from GNSS observations,” in *Atmospheric Remote Sensing*, A. Kumar Singh and S. Tiwari, Eds., in Earth Observation. , Elsevier, 2023, pp. 63–84. doi: 10.1016/B978-0-323-99262-6.00022-5.

[45] A. Elsayed, A. Sedeek, M. Doma, and M. Rabah, “Vertical ionospheric delay estimation for single-receiver operation,” *Journal of Applied Geodesy*, vol. 13, no. 2, pp. 81–91, Apr. 2019, doi: 10.1515/jag-2018-0041.

[46] “IRI | instant run | CCMC.” Accessed: Oct. 25, 2023. Available: https://kauai.ccmc.gsfc.nasa.gov/instantrun/iri/

[47] “What is the solar cycle? | NASA space place – NASA science for kids.” Accessed: Oct. 25, 2023. Available: https://spaceplace.nasa.gov/solar-cycles/en/

INITIAL DISTRIBUTION LIST

1. Defense Technical Information Center
   Fort Belvoir, Virginia

2. Dudley Knox Library
   Naval Postgraduate School
   Monterey, California